12-2017

Model Predictive Power Management of a Hybrid Electric Propulsion System for Aircraft

Tyler J. Wall
Western Michigan University, tjw0509@msn.com

MODEL PREDICTIVE POWER MANAGEMENT OF A HYBRID ELECTRIC PROPULSION SYSTEM FOR AIRCRAFT

by

Tyler J. Wall

A thesis submitted to the Graduate College
in partial fulfillment of the requirements
for the degree of Master of Science in Engineering
Aerospace Engineering
Western Michigan University
December 2017

Thesis Committee:

Richard T. Meyer, Ph.D., Chair
Peter A. Gustafson, Ph.D.
Tianshu Liu, Ph.D.

MODEL PREDICTIVE POWER MANAGEMENT OF A HYBRID ELECTRIC PROPULSION SYSTEM FOR AIRCRAFT

Tyler J. Wall, M.S.E.

Western Michigan University, 2017

This work presents the switched optimal power flow control for an aircraft with a hybrid electric propulsion system. The propulsion system is a switched system that operates in either of two modes: (i) battery discharging and electric motor propelling and (ii) battery charging and electric motor generating. The aircraft model and components that form the hybrid propulsion system are modeled as either an algebraic power source/sink or as a dynamic model with appropriate power and state interconnections. With the system model defined, a model predictive control power management strategy is set fourth which minimizes a performance index that includes altitude and velocity tracking errors, fuel use, and battery charge level. The switched system model predictive control problem is solved using an embedding approach that relaxes the discrete-valued mode control variables to continuous-valued ones. The solution of the continuous-valued problem results in the optimal power flow which reasonably tracks desired flight profiles while considering the efficient use of the hybrid powerplant. The proposed power management is demonstrated with an aircraft based on the Cirrus SR-20.

ACKNOWLEDGMENTS

This thesis would not have been possible without the guidance of my committee chair, Dr. Richard Meyer. I thoroughly enjoyed the partnership realized during the course of my graduate studies and his encouragement to excel in my work as a practicing engineer. I also would like to thank Dr. Peter Gustafson and Dr. Tianshu Liu for their willingness to serve on this thesis committee and for their influence throughout my engineering studies. In addition, I owe my deepest gratitude to my family for their support, love, and counsel during my academic career. My mother and father have been instrumental in my personal and professional development for which I owe them an immeasurable amount of gratitude. Further, I acknowledge my paternal grandparents for not only their incredible amount of passion and commitment towards my success, but also for opening their home for me to grow and share in many memories throughout my life. I cherish the many friendships and experiences I gained in, and prior to, my collegiate career and am thankful for the impact they have had on me.

Tyler J. Wall

TABLE OF CONTENTS

Table Of Contents–Continued

CHAPTER

Table Of Contents–Continued

CHAPTER

LIST OF TABLES

LIST OF FIGURES

LIST OF ABBREVIATIONS

HEP	Hybrid Electric Propulsion
UAV	Unmanned Aerial Vehicle
ICE	Internal Combustion Engine
BSFC	Brake Specific Fuel Consumption
ED	Electric Drive
BAT	Battery (Lithium-Ion)
CVT	Continuously Variable Transmission
J	Inertia
DOF	Degree of Freedom
MPC	Model Predictive Control
PI	Performance Index (Objective / Cost Function)
SR-20	Cirrus Design SR-20 Aircraft Model
P	Power
Q	Torque
R	Gear Transmission Ratio
η	Efficiency
V	Aircraft True Airspeed

List of Abbreviations–Continued

α	Aircraft Angle of Attack
θ	Aircraft Body Pitch Angle
$\hbar$	Aircraft Altitude
C	Non-dimensional Coefficient
$\overline{W}_{Bat}$	Battery State-of-Charge
δ_T	ICE Throttle Angle
ω	Angular Velocity
ξ	Propeller Advance Ratio
λ	Mode Switch Vector
x	State Vector
u	Control Vector
y	Algebraic Variable Vector
μ	PI penalty

Sub/Super-script

0	Initial / No load
ζ	ED/Battery mode (Discharge-Propel = 0 or Charge-Generate = 1)
∞	Far field scalar quantity
$*$	Optimal Value
i	Model or component (ICE, ED, etc.)
i, j	Model or component i in power mode j

Power Modes

M	Mechanical
E	Electrical
p	Propelling (ED)
g	Generating (ED)

CHAPTER 1

INTRODUCTION

Diminishing fossil fuel resources and increasing concerns over aircraft propulsion system emissions, noise, safety, and performance are reshaping aerospace technologies [1]. Over the next two decades, energy consumption in the aviation community is expected to increase by 11%, equivalent to 88 TWh [2]. To address fuel consumption and environmental concerns, NASA has set goals for aircraft technologies that aim to reduce noise and carbon emissions within the next twenty years by 55 dB and 75%, respectively, using today's transport airliners as the baseline [3–5]. Other national regulatory bodies and international aviation associations have similar outlooks and goals for the aircraft industry [6].

Historical trends in the general aviation (GA) market are provided in the General Aviation Manufacturers Association (GAMA) annual statistical databook and outlook [7]. Total fuel consumption and flight hours of GA aircraft has decreased in recent years. Despite this, nearly 190 million gallons of fuel was consumed by GA in 2015 alone. A typical piston driven aircraft consumed just under thirteen gallons of fuel per flight hour. Additionally, the International Civil Aviation Organization (ICAO) set goals in 2016 for the aviation community to improve fuel efficiency 2% per year from 2010 to 2020, achieve carbon-neutral growth from 2020 onward, and reduce CO_2 emissions to 50% of the 2005 value by 2050. In order to meet the ICAO, GAMA, and NASA goals, comprehensive improvements to existing aircraft propulsion systems must be explored.

The automotive industry has experienced tremendous growth in hybrid and all-electric powertrains. Similar concepts are being studied and implemented on unmanned aerial vehicles (UAVs), GA craft, and commercial airliners [8,9]. Hybrid electric propulsion (HEP) systems allow increased aircraft fuel economy, lower emissions, reduced takeoff and landing noise, higher system reliability, and improved operational capabilities. Some recent HEP powered UAVs and GA

Figure 1.1: DA36 E-Star 2 Hybrid aircraft [12]

aircraft have demonstrated nearly 50% and 40% fuel consumption reduction, respectively [10]. Widespread HEP powered flight and full-electric flight are thought to be achievable in the next seven years if battery technology, in terms of energy density, continues to improve at the same rate as it has over the past thirty years [11].

1.1 Hybrid Electric Aircraft Research and Demonstrators

Past UAV HEP research has primarily investigated their feasibility, design, and experimental implementation. In 1999, interest in high-altitude long-endurance UAVs led to the development of a hybrid solar array and internal combustion engine (ICE) configuration in which the solar array provides power during the day and the ICE provides power at night [13]. In the mid-2000s, further research into hybrid UAVs for the military conducted by Harmon [14–17] and Hiserote [18] provided sizing and control strategies for HEP systems. In military applications, hybrid UAVs not only provide reduced fuel use and emissions but also have the capability to significantly reduce heat signatures and noise with the utilization of electric motors [18].

In terms of manned aircraft, several hybrid and full-electric aircraft have been built [6]. The Alatus by Robertson was demonstrated in 2010 followed by another HEP aircraft, the EcoEagle, in 2011 [10]. In 2013, the Diamond Aircraft Company, along with with Airbus and Siemens, developed the DA36 E-Star 2, seen in Figure 1.1 [19]. The E-Star 2 claims to decrease fuel consumption

Figure 1.2: SUGAR Volt commercial HEP aircraft [23]

and carbon emissions by 25% when compared to the non-hybrid DA36. Recently, Friedrich and Robertson [8, 10] successfully operated a 210 kg light-sport HEP powered aircraft, named the SOUL, which is a modified version of the ICE powered SONG airframe by Gramex. In 2016, the HYPSTAIR project became the most powerful HEP aircraft in its category by delivering 200 kW in ground testing [20, 21]. The Airbus E-Star, E-Fan series, and E-Thrust programs [4] and NASA SCEPTOR [22] projects are also recent examples of manned HEP demonstrator aircraft.

HEP has also been explored for the commercial transport sector. Boeing, General Electric, and the Georgia Institute of Technology proposed a short-range transport called SUGAR (Subsonic Ultra Green Aircraft Research) shown in Figure 1.2 [23, 24]. It combines a hybrid gas turbine powerplant and improved aerodynamics to achieve improved fuel efficiency. The SUGAR project estimates that fuel savings for commercial aviation can reach up to 70% through HEP. Additionally, Zunum Aero is proposing HEP technology for different sized passenger aircraft. This project, sponsored by Boeing and JetBlue, aims to introduce HEP technology to the commercial market in the next five years with the goal of eliminating aviation emissions for short-haul flights; accounting for roughly 40% of all aviation emissions. As HEP technology improves, the Zunum HEP system will rely less on fuel and more on electric, with the end goal of an all-electric aircraft within twenty years as stated in their "hybrid-to-electric" proposal [20, 25]. Several researchers have also investigated conceptual commercial transports and offer sizing and optimization approaches in this sector [6, 10, 26]. In general, large, long-range, commercial aircraft like the 777 or A330, are less likely to realize as high of fuel savings as GA, UAV, and small commercial aircraft largely due to the weight of battery effect on aircraft performance; e.g. range, payload, and/or endurance.

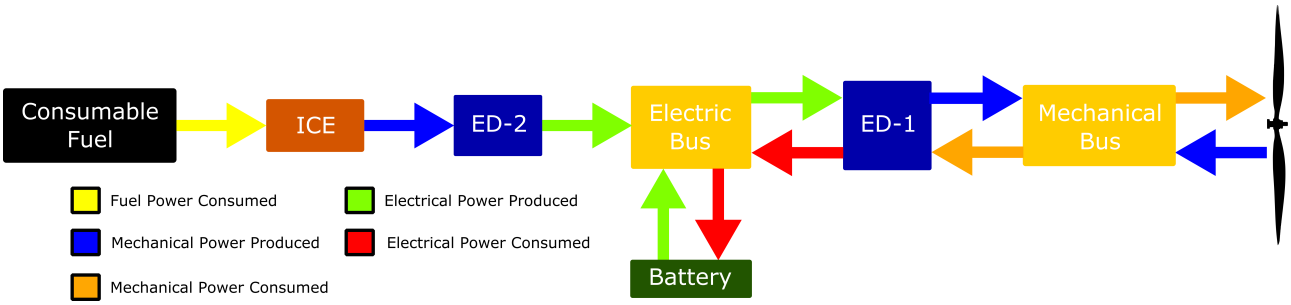

Figure 1.3: Series HEP configuration

1.2 Hybrid Power System Architectures

The generalized HEP system herein includes an ICE and its fuel; electric drives (EDs) that behave as a motor and/or generator; electrical energy storage system, e.g., battery pack; electrical bus to route electrical power; and mechanical bus, e.g., a transmission, to route power between the propeller and other mechanical sources and sinks. These components and their connections are similar to automotive applications. However, due to the sensitivity to size and weight and different missions introduced with aircraft applications, the benefits and drawbacks of each configuration are magnified [9]. HEP systems are normally configured in (i) series configuration, (ii) parallel configuration, and (iii) series-parallel / power-split configuration.

In a HEP series configuration, shown in Figure 1.3, ED-1, a motoring ED, is directly connected to the propeller though a mechanical bus, which is often a speed reducing transmission. Electrical power for the ED-1 is supplied by the battery, which is charged by ED-2, a generating ED, which is driven by the ICE. Additionally, the series configuration permits ED-2 generated power to bypass the battery and feed directly into ED-1. Applications involving low speed and high torque are best suited to incorporate the series configuration such as the DA36 E-Star 2 [19] and HYPSTAIR project [21].

In a HEP parallel configuration, displayed in Figure 1.4, the ICE and ED are connected via a mechanical bus to the propeller. This configuration has two modes of operation: (i) both the ICE and motoring ED drive the propeller while the battery discharges and (ii) the ICE drives both the propeller and the ED, behaving as a generator, to charge the battery. The mechanical bus generally consists of a mechanical transmission having a changeable gear ratio with output connected to the propeller and inputs from the ICE and ED. Further, there is either a clutch in the ICE or ED power

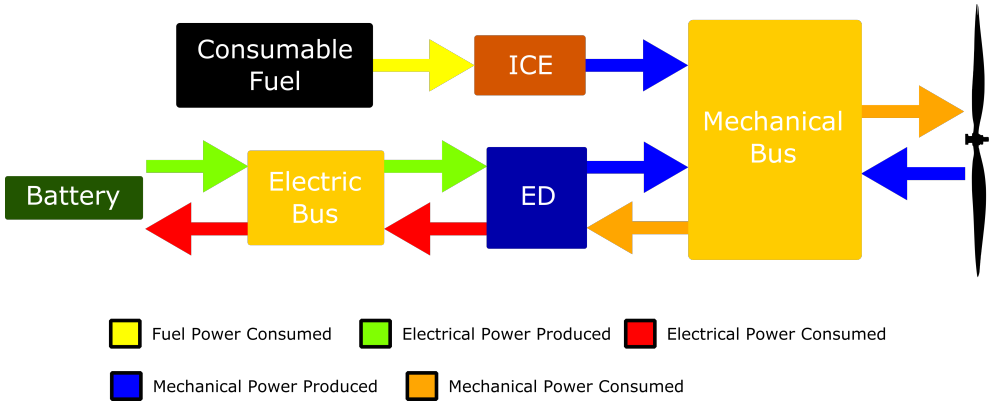

Figure 1.4: Parallel HEP configuration

flow path to couple/decouple it from the transmission or a clutch in both the ICE and ED power flow paths to couple/decouple them from the transmission. An example of the mechanical bus is a continuously variable transmission (CVT) combined with clutching to route power flows [19]. The option of two primary propulsion sources provides a safety redundancy for in case of HEP component malfunction. Many of the HEP systems for aircraft [10, 14, 19, 27] are based on the parallel architecture.

The last HEP system architecture considered is a series-parallel system, seen in Figure 1.5. This system is typified by the use of a planetary gear system to connect the ICE and EDs to the mechanical bus and consequently to the propeller shaft. Similar to a series hybrid, this configuration is installed with two EDs, one primarily for motoring, ED-1, and one primarily for generating, ED-2. In contrast to the series configuration, and similar to the parallel architecture, both the ICE and an ED can apply power to the propeller. Further, the series-parallel, unlike the parallel configuration, does not require clutching to transfer power between power sources, reducing complexity. The motoring ED can receive power directly from the generating ED, driven by the ICE, thus avoiding battery usage. A power-split configuration has been studied [17, 28], but not implemented in a HEP aircraft based on the literature surveyed; however, this configuration exists in terrestrial vehicles [9, 19].

Each HEP system configuration has advantages and disadvantages in terms of mass, cost, and power management complexity. The series and series-parallel configurations normally have greater mass than the parallel configuration for the same propeller power. This is because (i) the former two configurations have multiple EDs versus the single ED used in a parallel arrangement;

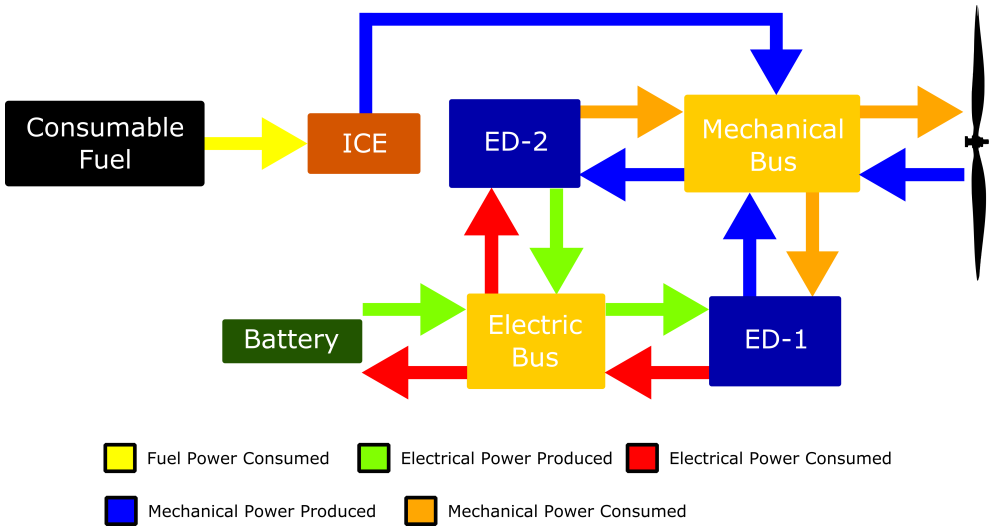

Figure 1.5: Series-parallel / power split HEP configuration

(ii) both the motoring ED and generating ED in the series configuration must be sized to provide the maximum propelling power, including efficiency losses in the numerous power conversions needed, while in the parallel configuration the ED is required to provide the difference in power between cruise and full propelling power available, i.e., less power is required, thus it is a smaller ED with less mass; and (iii) the series-parallel configuration requires a power split device unlike the parallel configuration.

Similar cost arguments follow from the mass comparison. Additional components as well as larger sized, i.e., higher power rated, components will normally lead to greater HEP cost. Thus, it is expected that the parallel configuration will be less costly than the series and series-parallel configurations.

Further, power management complexity increases with the number of potential power flow paths. The series configuration has the least number of potential power paths, in comparison, the most number of potential paths is the series-parallel configuration. Hence, power management complexity, in increasing order of complexity, is expected to be series, parallel, series-parallel configuration. HEP system mass, cost, and power management complexity are a few of the considerations for hybrid propulsion sizing and implementation. Terrestrial vehicles, which are not as mass-sensitive as aircraft, are currently trending towards a series-parallel architecture [9], while aircraft applications are trending toward the parallel one [18].

HEP aircraft are typically classified by a hybridization factor, which depends upon both

the ED and ICE maximum powers regardless of architecture. Typically, the hybridization factor is the maximum electric power to the propeller divided by the sum of the maximum ED and ICE powers. For example, a HEP with a hybridization factor of 0% indicates an ICE-only configuration, 100% is full electric, and 50% has equal power capabilities from both the ED and ICE. Alternate formulations of the hybridization factor are provided by Friedrich and Robertson [8] and by Lukic and Emadi [29].

1.3 System Component Modeling

Hybrid propulsion systems for aircraft are modeled in a similar fashion to hybrid powertrains in terrestrial vehicles [9]. HEP models are needed for simulation and control development over different operating scenarios. This section provides a review of modeling strategies for HEP system components, interconnections between components to form the system, and aircraft dynamics. Components modeled are the ICE, ED, battery, and aircraft. Interconnections include the mechanical and electrical buses.

1.3.1 Internal Combustion Engine

Past ICE models have been based upon conservation of power or a representation of the ICE ideal operating line (IOL). First, the conservation of power is applied to the ICE:

$$P_{ICE} = \eta_{ICE} P_{Fuel} - P_{Loss} = \eta_i (\dot{m}_f Q_{HV}) - P_{Loss} \tag{1.1}$$

where P_{ICE} is the mechanical power available for work, $P_{Fuel} = \dot{m}_f Q_{HV}$ is the fuel power delivered for combustion with $\dot{m}_f$ as the fuel mass flow rate, Q_{HV} is the fuel lower heating value, η_i is an operation dependent efficiency, and P_{Loss} are the losses, outside of combustion, associated with ICE operation. When $P_{Loss} = 0$ and η_{ICE} is an overall ICE power conversion efficiency, a model like that in Schoemann [30] is obtained. Further, when η_{ICE} is the fuel combustion efficiency, the result is the Willans line model [31]. The Willans line model is often used for extrapolating engine data down into low power regions as well as engine sizing via scaling of data from other engines. These models do not explicitly describe the air-to-fuel ratio, thermal effects, and other

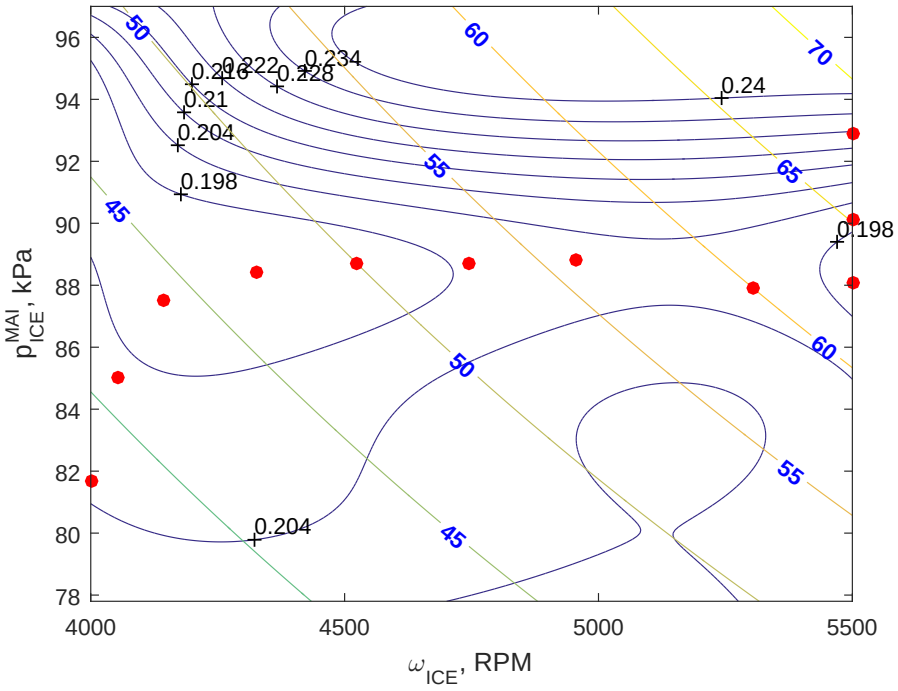

Figure 1.6: ROTAX 912iSc Sport IOL

engine parameters that affect performance. Additionally, automotive engine data can be applied to aircraft IOL creation, e.g., from ADVISOR [8, 31].

Another way to model the ICE is the IOL [8, 17, 18, 32]. Hung and Gonzalez [32] define the IOL as a smooth line connecting points which represent the torque and speed pairs at which fuel consumption is a minimum in steady-state operation. The benefit of IOL operation is that the ICE will operate with minimal fuel use provided it spends the majority of its operation in steady-state. Generation of an IOL begins with the ICE output torque versus angular speed plot. This plot is then overlaid with level curves of brake specific fuel consumption (BSFC), equal to $\dot{m}_f/P_{ICE}$, which are calculated at constant power values. Finally, a line is created that connects the angular shaft speed, ω_{ICE}, and minimum BSFC at that angular speed. The data from the IOL is often stored in a look-up table with inputs of engine torque and speed and output fuel consumption. Figure 1.6 is an example of IOL modeling for the ROTAX 912iSc Sport where IOL points are given as red dots and contours of BSFC are given in black and shaft power in blue. Once a plot of BSFC contours is established, power contour curves are superimposed on the plot. In Figure 1.6, red dots indicate sample IOL points for power contours in blue overlaid with BSFC contours in black. Note

that Figure 1.6 relates the manifold intake pressure p_{ICE}^{MAI}, rather than torque, to shaft speed. IOL development is further outlined in Hung and Gonzalez [32, 33] and Friedrich and Robertson [8].

An important distinction between terrestrial and aircraft ICE use is that power output varies with altitude. Also, wind and atmospheric effects, air density, temperature, and aircraft velocity can effect the ICE and should be considered for modeling of ICEs for HEP aircraft.

1.3.2 Electric Drive

An ED consists of an inverter and brushless DC motor that converts electrical power to mechanical power during motoring and vice-versa during generating. The motor has a rotor with magnets embedded in it, which is surrounded by non-rotating coils of wire called the stator. When the ED is used for motoring, electrical excitation of the stator causes the rotor to spin, thus converting electrical power to mechanical power. Conversely, when the ED is used for generating, the turning of the rotor results in electrical power being produced. The ED inverter here is bidirectional; its role is to transform DC power from an electrical source during motoring , e.g., the battery, into a form to be used by the ED, typically three-phase AC; in generating, the direction of power transformation is reversed. During the ED power conversion process, the magnitude of losses partially depends on whether the ED is motoring or generating.

Depending on the HEP system configuration and power demands, the EDs in the system are used to either turn the propeller and/or charge the battery. The ED can be modeled algebraically as an efficiency-based, input-to-output power converter

$$P_{ED,M} = \eta_{Inv}^{p} \eta_{ED}^{p} P_{ED,E} \tag{1.2}$$

$$P_{ED,E} = \eta_{Inv}^{g} \eta_{ED}^{g} P_{ED,M} \tag{1.3}$$

where $P_{ED,M}$ is the ED mechanical power, $P_{ED,E}$ is the ED electrical power, η_{Inv}^{p} and η_{ED}^{p} are the motoring inverter and motor efficiencies, respectively, and η_{Inv}^{g} and η_{ED}^{g} are the generating inverter and generator efficiencies, respectively. Motor efficiency values have been considered as functions of the ED rotor speed and motor input power with specific forms of the relationship obtained through least-squares data fits while the inverter efficiencies have been assumed to be constant [34, 35].

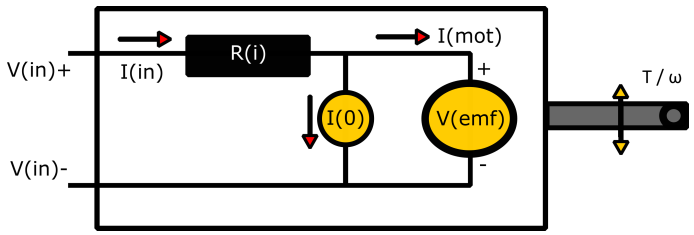

Figure 1.7: Equivalent circuit of an ED [30]

ED efficiency values have also been modeled using a loss function by McDonald [36]. The ED efficiency is

$$\eta_{ED,M} = \frac{\omega_{ED} Q_{ED}}{\omega_{ED} Q_{ED} + P_{ED,L}} \tag{1.4}$$

where ω_{ED} is the ED shaft angular velocity, Q_{ED} is the motor torque, and P_{ED}^{loss} is motor losses given by

$$P_{ED}^{loss} = C_0 + C_1 \omega_{ED} + C_2 \omega_{ED}^3 + C_3 Q_{ED}^2 \tag{1.5}$$

where the coefficients C_i for $i = 0, 1, 2, 3$ are determined from motor efficiency, torque, and rotor speed map data. This efficiency modeling approach was demonstrated for a UQM PowerPhase 125 ED powering a Cessna 172. The model offered by McDonald compared favorably to the manufacturer efficiency map.

Another approach to modeling input-to-output power transfer is look-up tables, which are used by Hung and Gonzalez [19]. They create a look-up table with the input as ED current which provides output of torque and power.

In contrast to efficiency maps and look-up tables, Schoemann and Hornung [30] model an ED using the simplified circuit modeled shown in Figure 1.7. This model was developed for a brushed motor but is said to offer reasonable accuracy for brushless types [37]. The result of the circuit analysis are relationships for the motor current I_{ED} and voltage E_{ED} as functions of torque

and speed:

$$I_{(in)} = Q_{ED}\frac{\omega_{ED}}{V_{(emf)}} + I_0 \tag{1.6}$$

$$E_{(in)} = E_{(emf)} + \left(Q_{ED}\frac{\omega_{ED}}{E_{(emf)}} + I_0\right)\cdot R_i \tag{1.7}$$

where $V_{(emf)}$ is the electromotive force, I_0 is the no-load current, and R_i is the motor internal resistance.

Altitude effects are not present in an ED as they do not breathe air and therefore power does not vary with altitude [38]. However, an ED's temperature should be regulated to avoid overheating.

1.3.3 Battery

The battery serves as a secondary energy source. The battery provides power to propel the aircraft though the ED or it can absorb and store excess kinetic energy for later use. Additionally, on-board avionics and other equipment are usually powered by the propulsion system. The relative power consumption between the avionics and other systems compared to the ED propulsive power requirements is assumed to be negligible and therefore the only effective battery power draw arises from the ED. A common assumption [10] is that HEP aircraft begins its flight with the batteries fully charged in order to maximize range and contribute to the high power demands of takeoff.

Lithium-polymer battery discharge modeling is presented in Hung and Gonzalez [19]. Specifically, they consider the state-of-charge, $\overline{W}_{Bat}$, i.e., the amount of energy in the battery, and the battery voltage on the terminals, E_{Bat}, as

$$\overline{W}_{Bat} = 100\left(1 - \frac{\int_0^t I_{Bat}dt}{W_{Bat}^{max}}\right) \tag{1.8}$$

$$E_{Bat} = E_{Bat,nom} - K\left(\frac{W_{Bat}^{max}}{W_{Bat}^{max} - I_{Bat}t}\right) + A_{Bat}e^{-B_{Bat}I_{Bat}t} \tag{1.9}$$

where I_{Bat} is the battery current, W_{Bat}^{max} is the maximum battery energy capacity, $E_{Bat,nom}$ is the nominal battery voltage, t is the current time elapsed since the battery began discharging, A_{Bat} and B_{Bat} are constants obtained from fitting experimental data, and K is the polarity voltage. Bradley

and Droney offer a similar modeling approach for a battery as well as a sizing algorithm based upon generalized discharge curves [23].

Agarwal et al. [39] provide an empirical, experimentally validated battery discharge and charge model as well as lifetime estimation for several battery chemistries including nickel-metal hydride and lithium-ion. Their dynamic model for the battery state-of-charge, $\overline{W}_{Bat}$, i.e., the normalized amount of energy is

$$\dot{\overline{W}}_{Bat} = -\frac{d_2^{\zeta}}{W_{Bat}^{max}}(P_{Bat,nom}^{\zeta})^2 - (\ln(-\overline{W}_{Bat} + d_1^{\zeta}) + 2d_2^{\zeta}P_{Bat,nom}^{\zeta} + d_3^{\zeta})\frac{P_{Bat}(t)}{W_{Bat}^{max}} \tag{1.10}$$

where P_{Bat} and $P_{Bat,nom}$ are the the battery discharge or charge power and nominal battery operating power, respectively. $d_i^{\zeta}, i = 1,2$ are parameters fit to discharge ($\zeta = 1$) battery efficiency map data and charge ($\zeta = 2$) battery efficiency map data.

Additional considerations for the battery include the option of regenerative charging through the propeller, weight impact on aircraft range, and thermal management of the battery and ED. Propeller windmilling has been investigated to provide regenerative charging during the aircraft descent phase, but has been found to not be a benefit as the additional drag due to windmilling would negate the energy gains [40]. The weight of batteries has a severe impact on aircraft performance and range and has been considered in many works. Pornet et al. [6, 24] treat the battery mass as a design variable and is therefore an optimized parameter in the total aircraft weight. A sensitivity study showed that battery specific energy has the largest impact on HEP performance. Decreasing the battery specific energy by 50% would reduce the potential fuel savings by nearly 50% as well and therefore gives rise to a fuel-burn benefit analysis to battery weight. Further, Moore [11] claims that an energy density of 400 Wh/kg and greater offers feasible HEP and all-electric implementation. Variations around typical energy density (200 Wh/kg) lead to a high sensitivity of aircraft gross weight. Last, thermal management of either the ED and battery has not been specifically studied as it relates to HEP. Considerations in the rapid changes attainable in altitude, and therefore the operating environment of the HEP system are lacking in current models.The effects of rapid environmental change, such as temperature, on components should be incorporated so that the system control can protect components and manage potential loss of performance. The largest concern in the literature for HEP and electric aircraft has focused primarily on battery weight and

thermal management has been a secondary factory. Robust battery and ED models should incorporate the aspects discussed herein.

1.3.4 Mechanical and Electrical Buses

The mechanical bus connects the mechanical power output/input devices with the propeller. The series, parallel, and series-parallel HEP systems considered herein have different mechanical buses. Series HEP systems [10, 41] usually employ a reduction drive or similar coupling device, i.e., electric clutch, between the motoring ED and propeller because of their simplicity and low mass. The generic reduction drive model is

$$\omega_{Prop} = R_{GR}\omega_{ED} \tag{1.11}$$

$$P_{Prop} = \eta_{RD}P_{ED,M} \tag{1.12}$$

where R_{GR} is gear ratio from ED-1 to the propeller, η_{RD} is the drive's power transfer efficiency, and ω_{Prop} is the propeller angular velocity.

A parallel hybrid mechanical bus connects the ICE, ED, and propeller together with a transmission, e.g., ones with fixed gear ratios or CVT. Further, the mechanical bus has either (i) a clutch in the ICE or ED power flow path to couple/decouple it from the bus or (ii) a clutch in both the ICE and ED power flow paths to couple/decouple them from the bus. Power flow and angular velocity modeling of the mechanical bus is similar to that in series hybrid.

$$\omega_{Prop} = R_{MB,ICE}\omega_{ICE} \tag{1.13}$$

$$\omega_{Prop} = R_{MB,ED}\omega_{ED} \tag{1.14}$$

$$P_{Prop} = \eta_{MB,ICE}P_{ICE} + \eta_{MB,ED}P_{ED,M} \tag{1.15}$$

where $R_{MB,ICE}$ is the gear ratio from the ICE to the propeller, $R_{MB,ED}$ is the gear ratio from the ED to the propeller, $\eta_{MB,ICE}$ is the power transfer efficiency from the ICE to the propeller, and $\eta_{MB,ED}$ is the power transfer efficiency from the ED to the propeller. Note that (1.13) holds only when the ICE is connected to the bus, e.g., no clutch or when a connecting clutch is closed. Similarly, (1.14) holds only when the ED is connected to the bus.

The parallel HEP mechanical bus by Hung and Gonzalez [19] employs a CVT with a clutch, which allows for an infinite number of speed ratios between the propeller shaft, ICE, and ED. For a CVT transmission in a parallel HEP, the angular acceleration of the propeller is

$$\dot{\omega}_{Prop} = \frac{Q_{Prop} + R_{CVT}(Q_{ICE} + Q_{ED}) - \dot{R}_{CVT}\omega_{ICE}(J_{ICE} + J_{ED})}{J_{Prop} + R_{CVT}^2(J_{ICE} + J_{ED})} \tag{1.16}$$

where J_{Prop}, J_{ICE}, and J_{ED} are the mass moment of inertia of the propeller, ICE, and ED, respectively, and R_{CVT} specific to their system is $\omega_{ICE}/\omega_{Prop}$. In contrast, Harmon [16] uses a gear reduction drive as the transmission in the parallel HEP mechanical bus.

In a series-parallel configuration, a planetary gear set connects a generating ED, motoring ED, ICE, and propeller to the motoring ED rotor shaft. Specific to the planetary gear system, the sun gear is attached to the generating ED, the ring gear is connected to the motoring ED, and the planetary gear carrier is secured to the ICE. Olsen et al. [28] observe that these types of transmissions are popular in automotive hybrid vehicles but pose weight, and therefore fuel consumption and complexity concerns for HEP aircraft applications. They model the angular velocities in this type of mechanical bus as

$$\omega_{ED-1} = \left(1 + \frac{r_s}{r_r}\right) \cdot \omega_{ICE} - \frac{r_s}{r_r}\omega_{ED-2} \tag{1.17}$$

$$\omega_{ICE} = \frac{r_s\omega_{ED-2} + r_r\omega_{ED-1}}{r_r + r_s} \tag{1.18}$$

where ω_{ED-1} is the angular velocity of the motoring ED, ω_{ED-2} is the angular velocity of the generating ED, r_s is the radius of the sun gear, and r_r is the radius of the ring gear. (1.19) provides the power summation for this specific bus.

$$P_{Prop} = \eta_{PG,ED-1}P_{ED-1,M} + \eta_{PG,ED-2}P_{ED-2,M} + \eta_{PG,ICE}P_{ICE} \tag{1.19}$$

where $\eta_{PG,ED-1}$, $\eta_{PG,ED-2}$, and $\eta_{PG,ICE}$ are power conversion efficiencies of the motoring ED, generating ED, and ICE for the planetary gear setup, respectively.

The electrical bus serves as the power transfer point between the battery and any EDs. The batteries and any EDs are normally connected to the electrical bus via bidirectional DC-DC

converters. The converters have been modeled with constant efficiencies that include electrical bus losses as well [34, 35]. The result is that the electrical bus is treated as having unit power transfer efficiency and the power flow across the electrical bus is conserved.

1.3.5 Aircraft Dynamics

The equations of motion for a fixed-wing aircraft are unaffected by the introduction of HEP. Depending on the degree of freedom (DOF) of the dynamics, aircraft motion can be modeled as either a point mass, 3-DOF or 6-DOF system. Classic aerodynamic and performance relationships relate the aircraft free stream velocity V_∞, thrust T, and propeller shaft power P_{ps} as given in (1.20):

$$V_\infty = \frac{\eta_{Prop} P_{ps}}{T} \tag{1.20}$$

where η_{Prop} is the propeller power conversion efficiency. Similar methods of aircraft modeling and flight performance are utilized in HEP studies.

Harmon [15] models aircraft as a point-mass

$$0 = L - mg\cos(\gamma) \tag{1.21}$$

$$m\frac{dV_\infty}{dt} = \frac{\eta_{Prop} P_{Ps}}{V_\infty} - D - mg\sin(\gamma) \tag{1.22}$$

where m is the mass of the aircraft, L is the total lift force, and D includes some portion of the total lift at some nonzero γ, the climb angle, and is the sum of the parasite and induced lift drag coefficient, the latter depending largely on aircraft velocity and weight. 6-DOF aircraft dynamics similar to that in Stevens [42], Schmidt [43], and Etkin [44] are considered in Friedrich and Robertson [10, 45] and in Hung and Gonzalez [33]. For their studies, the simulation software, X-Plane, MATLAB AeroSim Blockset, or similar Simulink models incorporate these equations of motion. This approach is also found in the HYPSTAIR project [21]. Details of the 6-DOF models are not listed due to space constraints, but are documented in the references.

Further, the propeller efficiency relationships needed in the this section can be found in standard aerodynamics texts or software [46–48]. Turbine thrust relationships can be found similarly.

1.4 Methods of Control for Power Flow Management

A HEP system needs some sort of control to coordinate the power flow magnitudes and directions. Of the literature surveyed, three prominent control strategies have been investigated for HEP control: Rule-Based, Fuzzy Logic, and Artificial Neural Network.

1.4.1 Rule-Based Control

Rule-based (RB) control is usually implemented in the form of IF <conditions> THEN <result-1> ELSE <result-2> rules based upon expert knowledge that are often used in HEP systems for their reliability, simplicity, and ease of implementation [19]. The intent of the rules is to keep the ICE operating at high efficiency while still providing the demanded torque and speed at the propeller for flight. The complexity of RB control is proportional to the number of rules developed. Harmon et al. [15–17] developed RB control for a parallel HEP with inputs of demanded propeller torque and angular velocity. The requirements at the propeller are turned into ICE operating requirements and if the torque demand results in operation at or below the IOL, then only the ICE is used. If more than the torque at the IOL is requested, then an ED supplies the torque difference up to its maximum output. However, if meeting the demanded torque results in more than that can be supplied by the ICE operating on the IOL and maximum ED output, then the ICE is operated above the IOL to make up the difference.

A similar RB control that attempts to keep the ICE operating on the IOL to promote fuel efficiency is used by Hung and Gonzalez [19]. They also propose ED-only operation rules for times of silent operation, such as when engaged in surveillance.

RB control is also employed by Friedrich and Robertson [8, 10] in a parallel HEP. This RB controller contains three operating modes which are chosen based on the various ranges of the battery state-of-charge: ICE-only, ICE and motoring ED, and ICE and generating ED. Specifically, ICE-only operation occurs if the battery is nearly depleted or full. The ICE and motoring ED will operate together when the state-of-charge is above 10% and the total power demand is above that on the ICE IOL. The ICE will drive the propeller and generating ED when the power demand is less than the ICE IOL power and the state-of-charge is less than 98%.

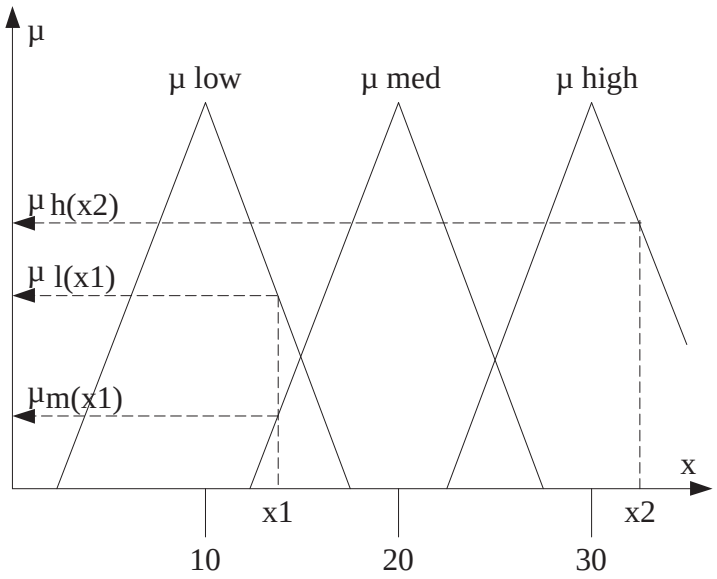

Figure 1.8: Fuzzy logic sets

1.4.2 Fuzzy Logic Control

Another approach to HEP system management is Fuzzy Logic Control (FLC). The process of applying FLC begins with finding a value's degree of membership in a fuzzy set. These membership degrees are then used as the conditionals in rules that are similar to those in RB control. The rules are combined via logical OR to obtain a fuzzy set output, which is then defuzzified to get crisp values that set system operation. For example, in Figure 1.8, membership functions $\mu_l(x)$, $\mu_m(x)$, and $\mu_h(x)$ are applied to x_1 and x_2 to find their degrees of membership in the sets. These membership degrees are then used as the conditionals in IF <conditions> THEN <result> rules which are typically based upon expert knowledge. The rules are evaluated by OR combination to obtain a fuzzy set output, which is then defuzzified to get crisp variables. FLC finds use in high-level supervisory control that cannot be achieved with classical control theory [16, 19]. However, as the number of rules in an FLC scheme increase, computation time increases in an exponential fashion.

Karunarathne et al. [49] developed two FLCs for a fuel cell-battery hybrid UAV. The battery state-of-charge and load power demand are inputs into the FLCs and the output of one FLC is the fuel cell operating level and the output of the other FLC is the battery power. The goal of the FLCs is to provide high energy efficiency of the HEP system.

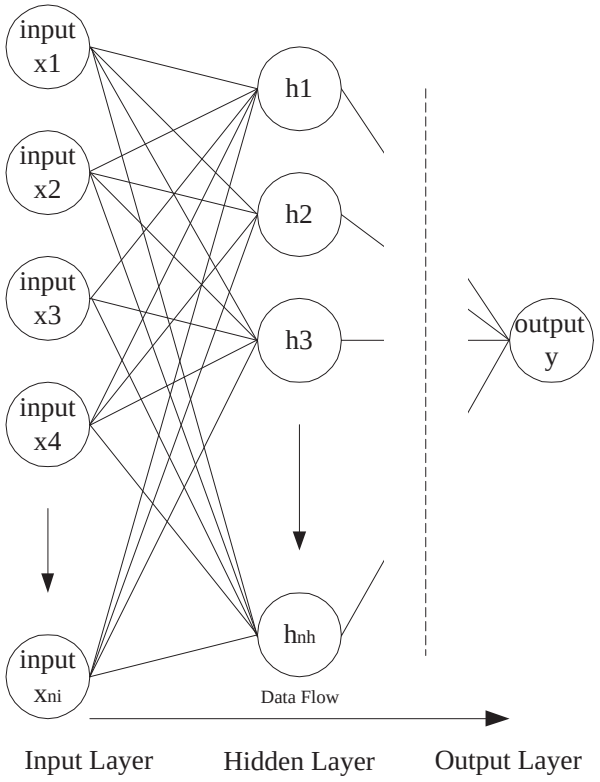

Figure 1.9: Neural network structures [50]

1.4.3 Artificial Neural Network Control

An Artificial Neural Network (ANN) has also been applied to HEP system control. Conceptually, the ANN attempts to mimic human reasoning using weighted summations. Inputs to a neuron, h_i in each hidden layer (there may be more than one neuron and hidden layer) undergo a weighted summation. Eventually the output layer is reached and the outputs from the last hidden layer are summed with weights after which a final activation function is applied as visualized in Figure 1.9. The neuron summation weights are found, i.e., learned through training which seeks to minimize the difference between desired and actual network output. ANNs have a low computational demand and short learning time [16].

Harmon et al. [15–17] created an ANN to control a parallel HEP. The ANN has inputs of propeller angular velocity, engine torque demand, and battery state-of-charge and output of commanded ICE torque. The ANN is trained to approximate an optimization that minimizes the instantaneous total power consumption of the ICE and motoring or generating ED. Whether or not

the form of the instantaneous power consumption considers motoring ED (battery discharge) or generating ED (battery charge power) depends upon the engine torque demand in relation to the IOL operating point.

1.4.4 Battery Power Operation

Aircraft HEP system battery management is normally classified in three forms: charge-sustaining (CS), charge-depleting (CD), and electric-only [14–19, 32, 33]. Specifically, a CS strategy attempts to maintain the battery state-of-charge at a specified level over the duration of the flight. In contrast, a CD strategy is typified by not recharging the battery over the flight; both the ICE and motoring-only ED provide propulsion. Finally, electric-only operation is a special case of the CD strategy where the ICE is off and the motoring-only ED is propelling the aircraft. A combination of these strategies may be used in each HEP aircraft flight depending on the HEP power management control. Flight missions known to be short in endurance can utilize a CD operation whereas longer missions will likely use a CD and/or CS strategy. A proportional-derivative control with input of battery state-of-charge is often used to modify torque demand in the RB control input so as to obtain battery recharge when the mission profile requires it.

1.5 Test Flight Profiles

Several different flight profiles have been explored to test HEP systems and their control. Two Intelligence-Surveillance-Reconnaissance (ISR) scenarios are simulated by Harmon et al. [14–17] to test their parallel HEP powered UAV: one with a one hour endurance and the other with a three hour endurance. These scenarios are characterized by a large amount of flight time spent in loiter mode where the aircraft travels around a fixed point at a fuel minimizing airspeed to collect data from on-board sensors. Simulation results show that the one hour flight with RB control and ANN control managed HEP system uses 65% and 67% less energy (combined fuel and electrical), respectively, than an ICE-only UAV. The three hour ISR flight achieves 34% and 38% energy savings with RB control and ANN control, respectively, compared to ICE-only operation.

Hung and Gonzalez [19] simulate a 15 km looped flight path with dedicated waypoints to test their Aerosonde UAV with a parallel HEP system and RB control. These waypoints incorporate

common military UAV operations consisting of climb, cruise, loiter, and descend. Results show the HEP equipped UAV achieves a 6.5% fuel savings over ICE-only powered flight.

Next, Friedrich and Robertson [10] simulate various flight profiles in order to validate a parallel HEP system under RB control. Two simulated flight paths over a 87 km course were developed; one at a constant altitude and varying speeds at cruise, and the other at various altitudes during cruise and at varying speeds. For the first flight profile, they obtained maximum fuel and energy savings of 35% and 31%, respectively, compared to the ICE-only driven aircraft. Over the second flight profile, a maximum fuel savings of 37% and energy reduction of 29% were observed. Friedrich and Robertson also performed scaling of their HEP system to investigate UAV and commercial transport feasibility. The UAV test flight profile was similar to that of the three hour ISR by Harmon et al. [14–17] described above. Calculated fuel savings are 47% for their UAV. Further, a Boeing 737-800 commercial transport is simulated with a HEP system. The tested flight scenario is a two hour, medium range mission to include a takeoff, climb, descent, and landing common to airline routes. In this scenario, a 10% fuel savings was obtained. The SUGAR Volt HEP aircraft utilized a similar flight path representative of a 1700 km airline route. This profile demonstrated a 57% fuel burn reduction [4], indicating that traditional commercial airframes do not realize the high fuel savings of clean-sheet HEP-orientated aircraft designs.

1.6 Aircraft Design and Performance Considerations

Methods to calculate aircraft performance and sizing are affected by the introduction of HEP systems. Traditional aircraft design and performance considers the use of combustion-based propulsion systems where the consumable fuel is reduced over the duration of the flight, which leads to time varying aircraft performance metrics [24]. Additionally, during the aircraft design process, initial sizing of aircraft systems and structures are normally based on historical values and trends, which do not usually include consideration of electrical propelling power systems [47]. Moore and Fredrick [11] address several misconceptions about electrified flight design and performance: the design of electric aircraft is the same as for traditional aircraft; the comparison of electric and traditionally powered aircraft should be compared without regard to overall aircraft integration, i.e., on an isolated system basis; electric aircraft are not economically viable; electric

propulsion power supplies, e.g., batteries, do not offer comparable range; and electric propulsion is only suitable for large commercial aircraft far into the future. Further, several authors have addressed design and performance changes due to HEP aircraft.

Nam et al. [51] investigates power-based propulsion system sizing, which includes HEP systems, and its effect on aircraft design. In essence, this requires integration of multiple power paths, each potentially with its own unique characteristics, into aircraft design processes. They modify traditional weight fraction estimations to incorporate power path blocks that include energy storage such as a battery or fuel tank, power transfer, e.g., electrical to mechanical power conversion, and propulsion. This work signifies a transition from traditional thrust and fuel balance to power and energy balance which leads to the classification of energy availability on-board the aircraft as either consumable (fuel) or non-consumable (batteries). Energy from batteries is non-consumable because the mass of the batteries does not change in flight. Pornet [24] also details the relationships of propulsion systems for aircraft that extend beyond ICE-only systems. Jagannath et al. [4] provides a simplified weight fraction calculation for fuel burn for hybrid aircraft utilizing a jet turbine.

Next, Harmon et al. [17] proposes minimizing the power required, and consequently the thrust at the aircraft endurance speed for HEP sizing. Constraints included in the optimization are wing loading, aspect ratio, and required ICE power. The optimization leads to various aircraft design parameters such as wing area, stall speed, lift coefficient, etc. Harmon et al. perform the optimization for a UAV, however HEP systems for other aircraft types can be sized using similar optimization methods with appropriate changes in the minimization objective function and constraints.

A common metric to evaluate aircraft performance is range, χ. Range also serves to perform comparisons between HEP and non-HEP aircraft. For this reason, flight and mission profiles and objectives should be as similar as possible to provide a fair comparisons of χ. The effect of battery weight on range has been studied by Hepperle et al. [52]; they demonstrate the direct relationship between battery energy capacity to range. Further analysis has been conducted by Bagassi et al. [53] and Traub [54] which reinforce the impact of battery weight on aircraft range. Hepperle

provides a modified calculation of aircraft range given in (1.23):

$$\chi = E^* \eta_{HEP} \frac{L}{D} \frac{m_{Bat}}{W} \tag{1.23}$$

where E^* is the specific energy capacity of the battery, η_{HEP} is the battery to propulsion power transfer efficiency, given as 0.75, L/D is the aircraft lift-to-drag ratio, a measure of aerodynamic efficiency, m_{Bat} is the battery mass and W is the aircraft total weight. As stated in (1.23), χ is directly proportional to E^* and m_{Bat} and inversely proportional to the total aircraft weight. Also note that aerodynamic efficiency has an effect on χ and its choice can restore some range potentially lost due to the inclusion of a battery.

To further evaluate performance between HEP and non-HEP aircraft, Friedrich and Robertson [10] offer two additional metrics in their work; fuel savings (FS), and energy savings (ES). FS is the fuel consumption compared to a baseline combustion power source and ES is a value based upon FS and electrical energy consumed during flight that is replaced from the electrical grid:

$$FS = \left(1 - \frac{F_C}{F_{Ref}}\right) \cdot 100 \tag{1.24}$$

$$ES = \left(1 - \frac{F_C + (W_{Bat}^{max}(1 - \overline{W}_{Bat}(t_f))/\eta_{Grid})}{F_{Ref}}\right) \cdot 100 \tag{1.25}$$

where F_C is the fuel consumption during flight, F_{Ref} is the baseline fuel consumption for the same non-HEP aircraft, $\overline{W}_{Bat}(t_f)$ is the battery state-of-charge at the end of the flight assuming the batteries were initially fully charged, i.e., $W_{Bat}^{max} = 1$, and η_{Grid} is the battery charging efficiency.

1.7 Summary of Literature Survey

This literature survey presents the architecture, modeling, control, and impact of HEP power systems for aircraft. HEP systems, like terrestrial vehicles, have been configured in series, parallel, and series-parallel architectures; the first two being the most relevant in recent years. Research regarding HEP aircraft systems has largely focused on the UAV and GA market due to less restrictive flight requirements, lower design and cost risk, and higher fuel savings than what is possible for large HEP aircraft.

The modeling of the HEP system needs to be carefully considered because design and control decisions are often based on the output of the system model. Therefore, it is important to select application-appropriate models of the HEP components. At each point in time during flight of a HEP aircraft, the HEP controller needs to select the ICE and ED power flow direction and power flow magnitude. A common HEP control strategy is to attempt to operate the ICE on the IOL with consideration also given to the battery state-of-charge and ED capabilities. With regards to this, RB and ANN control are currently the most common approaches to manage the power flows in a HEP system. However, surveyed investigations show that ANN control achieves greater fuel and energy savings than RB control.

HEP systems will initially find application in short and medium range UAV and GA aircraft and are an intermediate step towards full electric flight. To achieve significant, segment-wide reductions in fuel consumption and emissions, research should focus on GA aircraft and small, short range commercial and regional aircraft. To date, the literature has demonstrated that a HEP system has not been modeled using supervisory-level, power flow behavioral models. Power flow and efficiencies are determined instantaneously and no consideration of the future impact of current control actions are considered. It has been shown that HEP aircraft have different operating modes, however these modes have not been explicitly modeled and can give rise to inefficiencies in power flow transformations as HEP component dynamics and efficiencies depend on the operating conditions. Therefore, a switched-system approach which provides an optimal power flow management has yet to be introduced.

1.8 Thesis Overview

This work considers the control of a HEP system in terms of optimal power management between the various components which make up not only the hybrid system, but also the aircraft and interconnections between flight dynamics and the propulsion system. A supervisory-level power management scheme is selected to accomplish this objective. The power management is based upon model predictive control of the switched mode HEP system where the modes are (i) battery discharging/motor propelling and (ii) battery charging/motor generating.

The modeling of the HEP system components is in given Chapter 2, then Chapter 3 presents

the model predictive and switched system optimal control methodology which is used to manage the power flow in the HEP system. Flight simulations are provided in Chapter 4 to illustrate the hybrid system control installed on a Cirrus SR-20 aircraft for a variety of flight profiles and validation cases. Finally, Chapter 5 summarizes the work and makes recommendations for future research and improvements in this field.

CHAPTER 2

MODELING OF HYBRID SYSTEM COMPONENTS

2.1 Introduction

The development of the HEP system herein is given in the following three sections: First, the components forming the system are modeled for use in a supervisory-level control scheme. Next, the aircraft chosen to be equipped with the modeled HEP system, the Cirrus SR-20, will be presented for use in a three degree of freedom simulation. In addition, the propeller is modeled which provides power as a function of aircraft and propeller speed. Last, the system is constrained to operating modes which have unique dynamics and algebraic power flow relationships.

2.2 HEP System Modeling

This section sets forth the models which form the HEP system. Of the three prominent HEP architectures widely used in industry, a parallel configuration is chosen for the HEP system herein due to its weight savings over series and series-parallel HEP configurations as both employ two electric drives, one strictly for propelling and one for generating. Components forming this HEP model are the ICE, ED, battery, and mechanical and electrical bus. In this HEP system, the battery has different discharging and charging dynamics and the ED has different propelling and generating efficiencies. Thus, the HEP is a switched system with two modes of operation: (i) battery discharging and ED propelling and (ii) battery charging and ED generating. In this section, non-switched and switched HEP component models are developed for use within a supervisory-level power flow management.

2.2.1 Internal Combustion Engine

The ICE takes energy-dense combustible fuel and converts chemical energy to mechanical power. The ICE selected for this system is modeled based on the ROTAX 912iSc Sport. This engine is offers a high power to weight ratio, favorable fuel efficiency, and is widely used in industry such as in newer light-sport aircraft like the ICON A5. The ICE delivers a maximum steady-state power output, $P_{ICE}^{out_{max}}$, of 72 kW at a maximum shaft speed, ω_{ICE}^{max}, of 576 rad/s [55]. Power output as a function of engine speed and manifold air intake pressure, p_{ICE}^{MAI}, is given by a power scaling function suggested by Lang [56] is:

$$\frac{P_{ICE}^{out}}{P_{ICE}^{out_{max}}} = \left(\frac{p_{ICE}^{MAI*} - a \cdot (p_{ICE}^{MAI*} - p_{ICE}^{MAI})}{p_{ICE}^{MAI*}} \frac{\omega_{ICE}}{\omega_{ICE}^{max}} \right)^{b} \tag{2.1}$$

where $p_{ICE}^{MAI*} = 97.4$ kPa, the rated manifold intake air pressure and a and b are coefficients to fit the model to specific engine maps. Based upon the engine full load power curve [55], the coefficients a and b are 1.10 and 1.23, respectively providing an R^2 of 0.95.

p_{ICE}^{MAI} can be related to δ_T leading to a direct relationship between the throttle position, δ_T, and P_{ICE}^{out} for a given ω_{ICE} though (2.1). The throttle position and manifold air intake pressure relationship is approximated from the data available from ROTAX engine user manuals as given in (2.2).

$$p_{ICE}^{MAI}(\delta_T) = -6.03\delta_T^2 + 53.3\delta_T + 50 \tag{2.2}$$

In addition to power output and throttle position mapping, the ROTAX 912iSc Sport operators manual also provides the data to develop a fuel efficiency model for the ICE. This is accomplished by utilizing fuel consumption data, $\dot{m}_f$, given as a function of p_{ICE}^{MAI} and ω_{ICE}. Specific pairs of p_{ICE}^{MAI} and ω_{ICE} provide a unique $\dot{m}_f$ which are used in (2.1) to calculate output power at that specific operating condition. P_{ICE}^{fuel}, the fuel power available for work, is of interest because it is related to fuel consumption, i.e. BSFC. P_{ICE}^{fuel} is calculated by multiplying BSFC by the lower heating value of gasoline, $44,400$ kJ/kg, and P_{ICE}^{out}. Therefore, P_{ICE}^{fuel} is a surrogate for $\dot{m}_f$; thus minimizing P_{ICE}^{fuel} later will be the same as minimizing $\dot{m}_f$. BSFC data is used to generate fuel power information at various engine speeds and throttle positions. The resulting engine map is generated by plotting BSFC as a function of p_{ICE}^{MAI} and ω_{ICE} as provided in Figure 2.1 which permits visu-

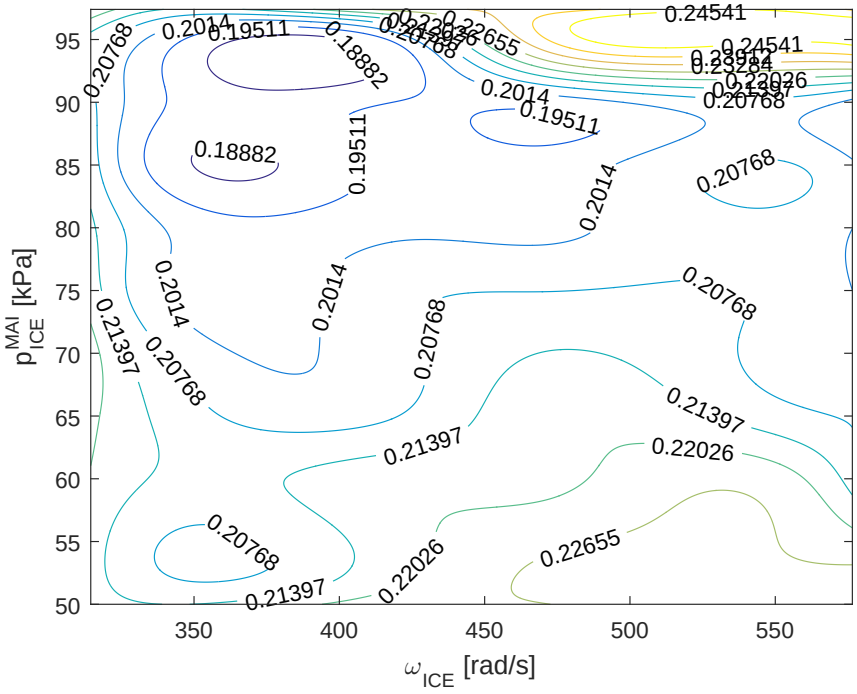

Figure 2.1: Approximated BSFC contours for the ROTAX 912iSc Sport

alization of contours of BSFC for different ICE operating points. Also, Figure 2.2 provides the P_{ICE}^{out} map as a function of δ_T and ω_{ICE}, which follow typical ICE power curve trends for similar domains.

Using (2.1) through (2.2), and data from the operators manual, P_{ICE}^{fuel} and P_{ICE}^{out} are fitted to a quadratic model in $\bar{\omega}_{ICE}$, the normalized ICE engine speed, and δ_T which is given in (2.3) and is favored for use in an optimization.

$$[\bar{P}_{ICE}^{out}, \bar{P}_{ICE}^{fuel}](\bar{\omega}_{ICE}, \delta_T) = a_0 + a_1\bar{\omega}_{ICE} + a_2\delta_T + a_3\bar{\omega}_{ICE}\delta_T + a_4\bar{\omega}_{ICE}^2 + a_5\delta_T^2 \tag{2.3}$$

where the output $\bar{P}_{ICE}^{out}$ is equal to $P_{ICE}^{out}/P_{ICE}^{out_{max}}$ and similarly for P_{ICE}^{fuel} for which $P_{ICE}^{fuel_{max}} = 220$ kW; are plotted in in Figures 2.3 and 2.4 . The fitting coefficients are listed in Table 2.1. The curve fit R^2 values are calculated for $\bar{P}_{ICE}^{out}$ as 0.99 and $\bar{P}_{ICE}^{fuel}$ as 0.97

The dynamic response of the ICE is approximated by modeling the change in throttle as a

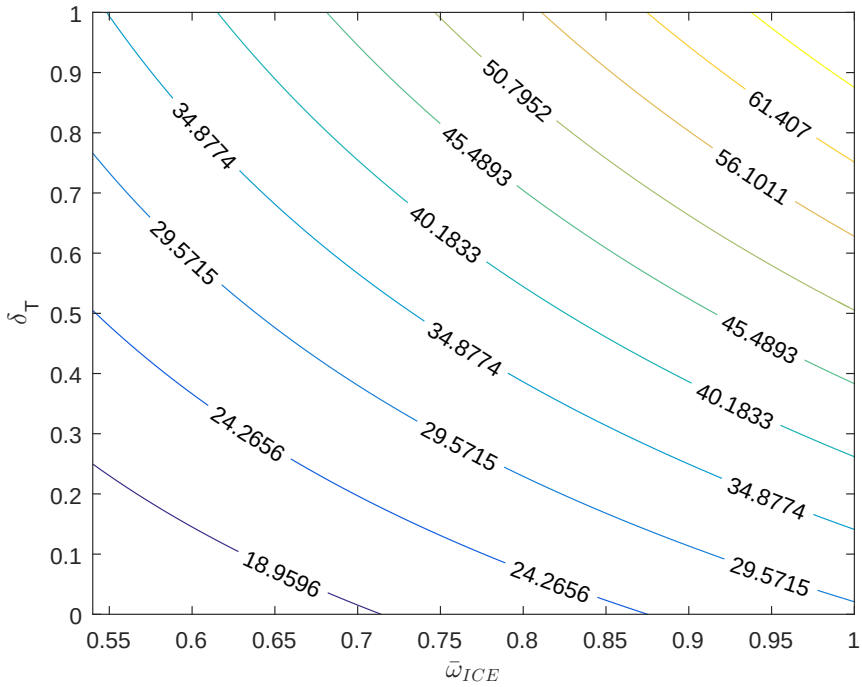

Figure 2.2: ICE shaft power output [kW] contours, based on ROTAX 912iSc Sport

Table 2.1: Curve fitting coefficients for the ROTAX 912iSc Sport ICE model

	a_0	a_1	a_2	a_3	a_4	a_5
$\bar{P}_{ICE}^{out}$	0.0	0.292	-0.073	0.689	0.104	-0.013
$\bar{P}_{ICE}^{fuel}$	0.205	-0.467	-0.641	0.943	0.223	0.288

first order lag differential equation:

$$\frac{d\delta_T}{dt} = \frac{1}{\tau_{\delta_T}}(-\delta_T + u_{\delta_T}) \tag{2.4}$$

where the throttle control is $u_{\delta_T} \in [0,1]$. $\tau_{\delta_T} = 0.25$s is the representative time constant of the throttle response approximated based on previous ICE modeling conducted by Meyer et al. [34]. Further, the efficiency of the ICE, η_{ICE} is given as the ratio of P_{ICE}^{out} to P_{ICE}^{fuel} which is also a function of δ_T and ω_{ICE}. For the ROTAX 912iSc Sport, the maximum η_{ICE} is 0.44; a reasonable value for high efficiency and high power to weight ratio aircraft ICEs. Note that this ICE model is representative of the ROTAX 912iSc Sport; the model is based upon the full-load power curve from the manufacturer.

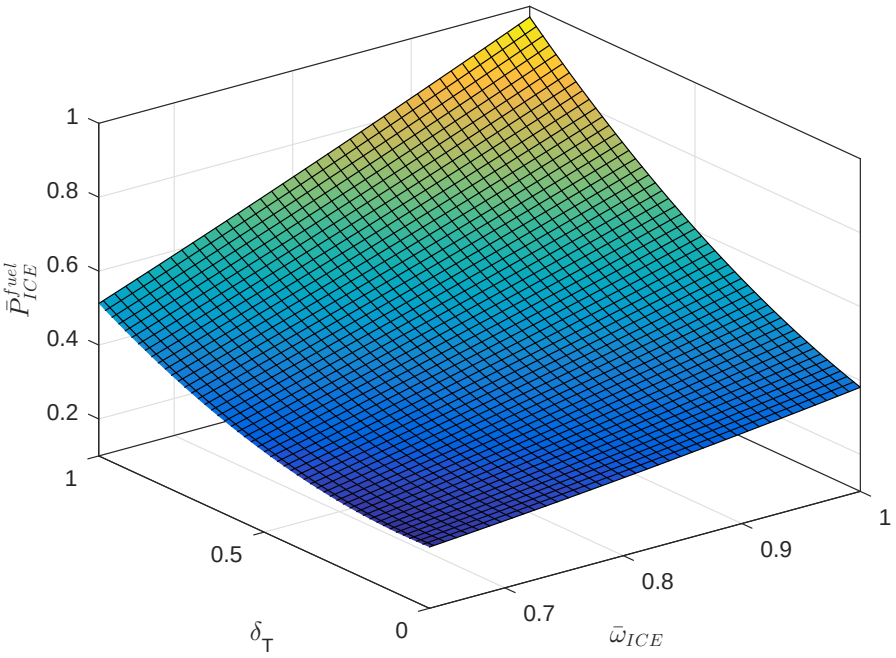

Figure 2.3: Normalized P_{ICE}^{fuel} curve fit as a function of $\bar{\omega}_{ICE}$ and δ_T

2.2.2 Electric Drive

The UQM PowerPhase 100 model by Meyer et al. [34] is employed in the ED system herein as it satisfies the power output requirement of the aircraft, notably at takeoff in combination with the ICE power output. The ED has maximum mechanical power output of 100 kW and maximum angular velocity of 470 rad/s. Also, the ED includes an the inverter which is a bidirectional DC-AC and is modeled by the propelling and generating inverter efficiencies, η_{Inv}^{p} and η_{Inv}^{g}, respectively, both assumed to be unity for simplification.

The ED is modeled during propelling as;

$$P_{ED,E}(t) = P_{ED,E}^{MAX,p}(\omega_{ED}) u_{ED}^{1}(t) \tag{2.5}$$

$$P_{ED,M}(t) = \eta_{ED}^{p}(\omega_{ED}) \eta_{Inv}^{p} P_{ED,E}(t) \tag{2.6}$$

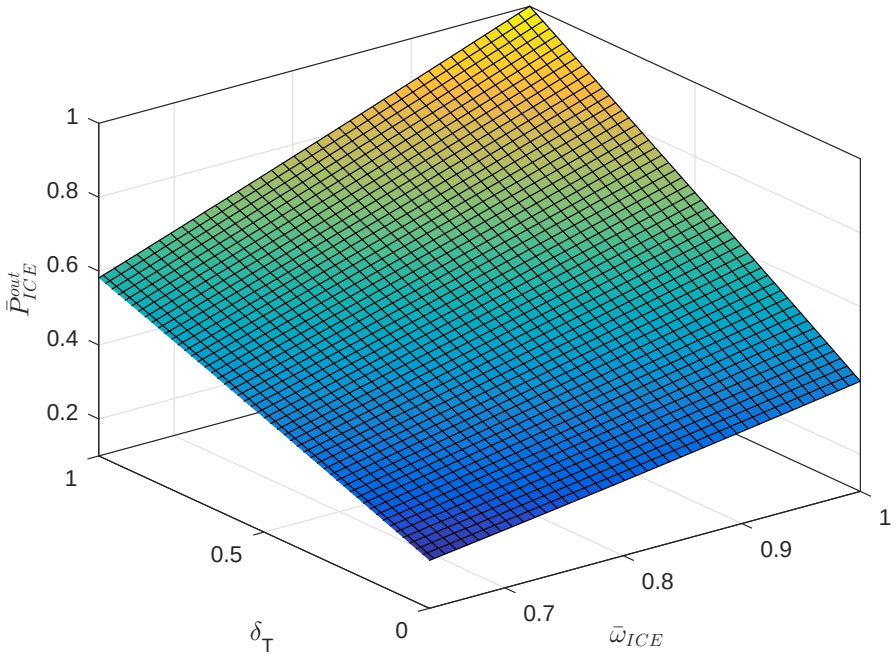

Figure 2.4: Normalized P_{ICE}^{out} curve fit as a function of $\bar{\omega}_{ICE}$ and δ_T

and during generating as;

$$P_{ED,E}(t) = \eta_{ED}^{g}(\omega_{ED})\eta_{Inv}^{g}P_{ED,M}(t) \tag{2.7}$$

$$P_{ED,M}(t) = P_{ED,M}^{MAX,g}(\omega_{ED})u_{ED}^{2}(t) \tag{2.8}$$

where $P_{ED,E}$ is the ED electrical power, and $P_{ED,M}$ is the ED mechanical power. The maximum generating mechanical power is given as $P_{ED,M}^{MAX,g}$ and the maximum propelling electrical power input is $P_{ED,E}^{MAX,p}$. $u_{ED}^{\zeta} \in [0,1]$ is the power modulating control input for propelling ($\zeta = 1$) and generating ($\zeta = 2$), ω_{ED} is the ED angular shaft speed and the propelling and generating power transfer efficiencies are η_d^p and η_d^g, respectively, which are fitted from manufacturer data and given in (2.9) and (2.10).

$$\eta_{ED}^{g}(\omega_{ED}) = 0.710 + 1.50 \cdot 10^{-3}\omega_{ED} - 2.62 \cdot 10^{-6}\omega_{ED}^{2} \tag{2.9}$$

$$\eta_{ED}^{p}(\omega_{ED}) = 0.802 + 7.59 \cdot 10^{-4}\omega_{ED} - 1.30 \cdot 10^{-6}\omega_{ED}^{2} \tag{2.10}$$

Again, utilizing manufacturer data curve fits, $P_{ED,M}^{MAX,g}$ and $P_{ED,E}^{MAX,p}$ are given in (2.11) and (2.12), respectively.

$$P_{ED,M}^{MAX,g} = \begin{cases} 0.550\omega_{ED}, & 0 \leq \omega_{ED} \leq 50\pi \\ 1.10\cdot 10^{-5}\omega_{ED}^3 - 1.13\cdot 10^{-2}\omega_{ED}^2 & \\ \quad +3.29\omega_{ED} - 1.94\cdot 10^2, & 50\pi < \omega_{ED} \leq \frac{200\pi}{3} \\ 100, & \frac{200\pi}{3} < \omega_{ED} \leq 150\pi \end{cases} \tag{2.11}$$

$$P_{ED,E}^{MAX,p} = \begin{cases} 3.49\cdot 10^{-2}\omega_{ED}^3 - 4.36\cdot 10^{-2}\omega_{ED}^2 + 1.5, & 0 \leq \omega_{ED} \leq 3 \\ P_{ED,M}^{MAX,g}/\eta_{ED}^p(\omega_{ED}), & 3 < \omega_{ED} \leq 150\pi \end{cases} \tag{2.12}$$

a small offset of 1.5 kW is added during propelling for $\omega_{ED} < 3$ rad/s so that $P_{ED,E}^{MAX,p}$ is non-zero for $\omega_{ED} = 0$. The small offset allows for the ED to drive the propeller from rest

2.2.3 Battery

The battery state of charge, $\overline{W}_{Bat}$, dynamic model is from Meyer et al. [34, 35]; the model is an expansion of an empirical, experimentally validated battery model from Agarwal et al. [39].

$$\begin{aligned} \dot{\overline{W}}_{Bat}(t) = \frac{1}{W_{Bat}^{max}}(d_2^{\zeta}(P_{Bat,nom}^{\zeta})^2 + 2d_4^{\zeta}(P_{Bat,nom}^{\zeta})^3 - [k^{\zeta}\ln(\overline{W}_{Bat} + d_1^{\zeta}) + \\ 2d_2^{\zeta}(P_{Bat,nom}^{\zeta}) + d_3^{\zeta} + 3d_4^{\zeta}(P_{Bat,nom}^{\zeta})^2]\cdot P_{Bat}(t)/n_{mod}) \end{aligned} \tag{2.13}$$

where P_{Bat} is the battery discharge or charge power, W_{Bat}^{max} is the maximum energy that can be stored in the battery, and $d_i^{\zeta}, i = 1,2$ are parameters fit to discharge battery efficiency map data ($\zeta = 1$, $k^1 = -1$) and charge battery efficiency map data ($\zeta = 2$, $k^2 = 1$). n_{mod} is the number of battery modules which form the entire battery pack itself.

The battery data provided by past modeling [34] is based upon the Saft 12Ah Lithium-ion modules. This approach requires that the various d_i^{ζ} given in (1.10) are per-module for P_{Bat} in

Watts. From past modeling d_i^ζ are calculated for discharging, $\zeta = 1$, d_1^1 is 3.91, d_2^1 and d_3^1 are $-8.85e-05$ and 2.57, respectively and d_4^1 is $2.85e-07$. For charging, $\zeta = 2$, d_1^2 is 25.7, and d_2^2 and d_3^2 are $1.4e-04$ and -2.27, respectively and d_4^2 is $2.36e-08$. Also required in the model, the per-module $P_{Bat,nom}$ is 370 W for $\zeta = 1$ and -370 W for $\zeta = 2$. W_{Bat}^{max} is $5.108e+05$ Ws, and the maximum discharge/charge power of the battery is 121/-121 kW ($\zeta = 1$ / $\zeta = 2$). The coefficients given assume operation of the battery in a standard atmosphere environment and the effects of temperature variations are neglected in order to avoid complicating the model as only the supervisory-level dynamics and conceptual principles are required in the scope of this work.

An example battery pack for a hybrid fuel-cell vehicle consists of 27 modules [34]. An integer number of battery packs is based upon 27 modules / pack. To adhere to weight and spacing limitations with the installation of batteries in place of fuel for an aircraft, $n_{mod} = 81$, representing 3 automotive hybrid battery packs. This battery pack formulation provides an initial model and can be refined further as needed based on simulation results because the model allows for n_{mod} as a design variable in the HEP system.

2.2.4 Mechanical and Electrical Bus

The mechanical bus connects the mechanical power output/input devices with the propeller. The parallel hybrid mechanical bus in the HEP system herein connects the propeller shaft to the ICE through a CVT and ED to the propeller shaft through a fixed helical gear ratio The mechanical bus has either (i) a clutch in the ICE or ED power flow path to couple/decouple it from the bus or (ii) a clutch in both the ICE and ED power flow paths to couple/decouple them from the bus. Herein, both the ICE and ED can idle while connected to the bus, i.e., the ICE can run at a minimum speed and the ED can operate at zero power, thus no clutch action is modeled. Additionally, keeping the ICE and ED connected provides an additional factor of safety if a sudden burst of power is needed to maintain flight.

As mentioned, the ED is connected to the propeller shaft via a fixed ratio gear set. The gear ratio is chosen to align the high efficiency region of the ED operation with the maximum speed of the propeller, which results in a gear ratio of 2; thus $\omega_{ED} = 2\omega_{Prop}$. Further, the gear set power transfer efficiency is taken as unity.

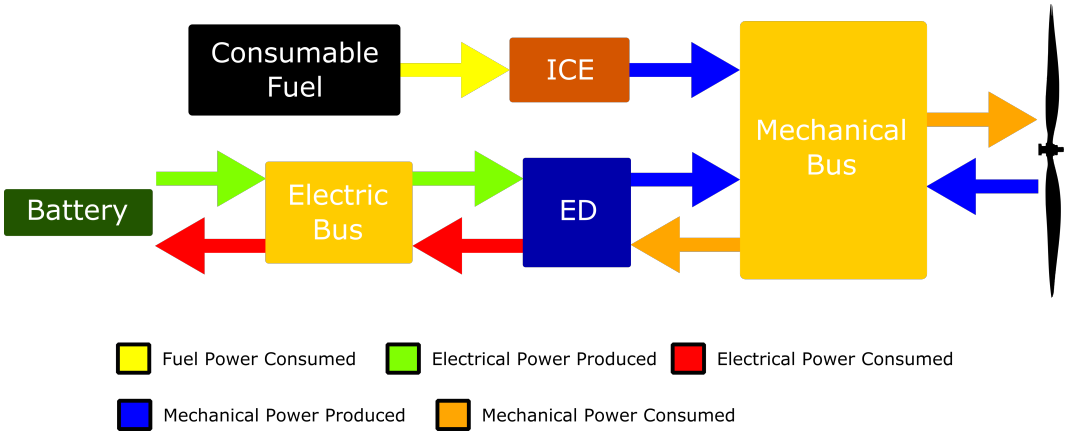

Figure 2.5: Parallel HEP system component architecture

The CVT gear ratio change is modeled here to approximate the dynamics demonstrated in Grzegozek and Szczepka [57]:

$$\dot{R}_{CVT}(t) = 0.45u_{CVT}(t) - 0.225 \tag{2.14}$$

where $u_{CVT} \in [0,1]$, the CVT control input, modulates the gear ratio change and $R_{CVT} \in [0.35,1]$ is the gear ratio: $\omega_{Prop}/\omega_{ICE}$. The range of R_{CVT} is chosen such that the maximum propeller speed can be provided at the minimum engine speed and vice-versa. Further, the CVT power transfer efficiency is $\eta_{CVT} = 0.95$ which is the approximate mean of reported values [58, 59]. Thus, the mechanical bus power connection for ED propelling is

$$P_{HEP}(t) = \eta_{CVT}P^{out}_{ICE}(t) + P_{ED,M}(t) \tag{2.15}$$

and for ED generating, the connection is

$$P_{HEP}(t) = \eta_{CVT}P^{out}_{ICE}(t) - P_{ED,M}(t) \tag{2.16}$$

where P_{HEP} is the mechanical HEP shaft power delivered to the propeller.

The mechanical bus dynamics are represented through deriving the torque balance on the propeller shaft similar to the model in Hung and Gonzales [32]. The propeller shaft power, P_{ps}, is the power required to obtain a specific propulsive thrust at ω_{Prop}. From mechanics, the sum of

the torques on a shaft is equal to the inertial load on the propeller shaft, J_{Prop}, times the angular acceleration of the propeller shaft, $\dot{\omega}$. J_{Prop} is large enough to ignore J_{ICE} and J_{ED}. Therefore, the mechanical bus dynamic response is

$$\dot{\omega}_{Prop}(t) = \frac{-P_{ps}(t) + P_{HEP}(t)}{\omega_{Prop}(t)} \cdot \frac{1}{J_{Prop}} \tag{2.17}$$

The electrical bus has been previously modeled by Meyer et al. [34, 35] and the same value is taken in this work; a constant efficiency; $\eta_{DCC} = 0.92$. When the battery is discharging, the ED is propelling, and the connection is

$$\eta_{DCC} P_{Bat}(t) = P_{ED,E}(t) \tag{2.18}$$

since greater electrical power needs to be supplied by the battery than the ED electrical power due to the power transfer efficiency of 0.92. For battery charging and ED generating, the connection is

$$P_{Bat}(t) = -P_{ED,E}(t)\eta_{DCC} \tag{2.19}$$

since the electrical power delivered by the ED must pass through the power transfer efficiency of the converter and therefore less power than that supplied by the ED is received at the battery. A negative is associated with (2.19) for use in the defined battery model where a negative P_{Bat} in (2.13) reflects the proper charging dynamics.

2.3 Flight Dynamics

An aircraft is modeled using longitudinal equations of motion (EOM). Given a rigid aircraft, motion is restricted to three degrees of freedom (DOF): pitch, θ, altitude, $\hbar$, and range, χ [42]. The flight dynamics of interest are only that of longitudinal motion which captures the necessary flight loads to provide an approximate model as these dynamics are what are common in safe, GA service; that is, wings-level, steady flight. This avoids complicating the model to require a full 6 DOF model which emphasizes higher-level aerodynamic modeling, i.e. lateral-directional EOM in addition to the longitudinal 3-DOF EOM.

The EOM for an aircraft are decomposed into forces in the direction parallel and perpendicular to the flight path [42, 46, 60]. Forces acting on the aircraft are L, D, M, and T, which are the total lift and drag force, moment, and propulsive thrust force, respectively. The longitudinal 3-DOF model to simulate a fixed-wing aircraft is:

$$\dot{V}_\infty(t) = \frac{-D(t)}{m} - g\sin(\gamma) + \frac{T(t)}{m}\cos(\alpha) \tag{2.20}$$

$$\dot{\alpha}(t) = \frac{-L(t) + mg\cos(\gamma) - T(t)\sin(\alpha)}{mV_\infty(t)} + q \tag{2.21}$$

$$\dot{\theta}(t) = q \tag{2.22}$$

$$\dot{q}(t) = \frac{M(t)}{J_{yy}} \tag{2.23}$$

$$\dot{\chi}(t) = V_\infty\cos(\gamma) \tag{2.24}$$

$$\dot{h}(t) = V_\infty\sin(\gamma) \tag{2.25}$$

where γ is the flight path angle, equal to $\theta - \alpha$, also described as the angle made between the aircraft body x-axis and the far field horizon. The angle of attack, α is the angle between the aircraft x-body axis and V_∞, the relative airspeed vector of the incoming air. q is aircraft pitch rate and m is the aircraft mass. The aircraft pitching moment of inertia, J_{yy}, is calculated from Roskam [61]

$$J_{yy} = \frac{\underset{\sim}{L}^2 m\bar{R}_y}{4} \tag{2.26}$$

where $\bar{R}_y$ is the radius of gyration based upon aircraft type and powerplant configuration and $\underset{\sim}{L}$ is the physical aircraft length. The L, D, and M, and T calculations are given as:

$$L(t) = (\bar{q})S_{ref}C_L = \left(\frac{1}{2}\rho_\infty V_\infty^2\right)S_{ref}C_L \tag{2.27}$$

$$D(t) = \bar{q}S_{ref}C_D \tag{2.28}$$

$$M(t) = \bar{q}S_{ref}\bar{c}C_M \tag{2.29}$$

$$T(t) = \frac{\eta_{Prop}P_{ps}}{V_\infty} \tag{2.30}$$

where $\bar{q}$ is the dynamic pressure, ρ_∞ is the free-stream air density, S_{ref} is the aircraft wing reference

area, the mean aerodynamic chord is $\bar{c}$.

C_L, C_D, C_M are the non-dimensional aerodynamic coefficients for L, D, and M, respectively, that include stability derivatives, denoted with subscripts paired to a respective coefficient, e.g., $C_{L_q} = dC_L/dq$. These coefficients are represented as a summation of component terms due to the current flight state, steady-flight terms denoted as initial values (ex: C_{L_0}) and δ_E, the elevator deflection angle in radians.

$$C_L = C_{L_0} + C_{L_\alpha}\alpha + C_{L_{\delta_E}}\delta_E + \frac{\bar{c}(C_{L_{\dot{\alpha}}}\dot{\alpha} + C_{L_q}q)}{2V_\infty} \tag{2.31}$$

$$C_D = C_{D_0} + \frac{1}{\pi eAR}C_L^2 \tag{2.32}$$

$$C_M = C_{M_0} + C_{M_\alpha}\alpha + C_{M_{\delta_E}}\delta_E + \frac{\bar{c}(C_{M_{\dot{\alpha}}}\dot{\alpha} + C_{M_q}q)}{2V_\infty} \tag{2.33}$$

where AR is the aspect ratio of the wing, the ratio of the wingspan b, squared, to S_{ref}. The Oswald efficiency, e, is a measure of how closely the wing lift force distribution matches that of an elliptical wing; which can be evaluated empirically [62].

This section has presented the 3-DOF model and the necessary aerodynamic model components to simulate a fixed-wing aircraft. This approach is valid for a wide variety of traditional and even modern aircraft. Once aircraft physical dimensions and aerodynamic properties, such as the wing airfoil and drag component buildup are known, direct substitution of those quantities into the 3-DOF model presented allows simulation unique to a given aircraft configuration. This approach is applied to the Cirrus SR-20 aircraft as detailed in the next section.

2.4 Modeling of the Cirrus SR-20 Aerodynamics, Stability, and Control

The aircraft chosen for the implementation of the HEP system herein is the Cirrus SR-20. The SR-20, seen in Figure 2.6 is a common GA, low wing, tractor-style propulsion configuration with a top speed of 100 m/s and seating up to five occupants. This aircraft is available in the Western Michigan University College of Aviation (WMU COA) fleet whose performance and stability formulations as well as accessible flight test data is available in WMU aerospace engineering course materials and through data provided by the WMU COA. The aerodynamic model variables described in the previous section are derived here from [42, 44, 46, 47, 60, 62, 63] and FAA doc-

Figure 2.6: The WMU Cirrus SR-20

umentation available online such as the Type Certificate Data Sheet (TCDS) [64, 65] and Pilots Operating Handbook (POH) [66].

The aircraft weight is fixed at 13.3 kN (3000 lb); the maximum takeoff weight defined in the POH. Any weight lower than the maximum takeoff weight results in improved fuel efficiency and performance; hence, the HEP system operates at takeoff weight throughout the flight which represents the maximum demand of the airframe and powerplant throughout the whole flight; any weight less than the maximum takeoff weight would result in improved flight performance and therefore the flight efficiencies calculated can only improve from what they are defined as in this work.

Physical properties of the aircraft can be obtained by using the POH which yield several variables for use in the 3-DOF model specific to the SR-20. $\bar{c}$ is 1.23 m and S_{ref} is 12.67 m^2 allowing b to be calculated as 10.71 m. Schmidt [43] provides two additional physical variables used in calculating stability derivatives; ε_α and $\bar{V}_h$. $\varepsilon_\alpha = d\varepsilon/d\alpha$ which physically represents the change in wing-induced downwash for use in variables involving the horizontal stabilizer aerodynamics which can be calculated from plots in Ektin [44]; ε_α=0.336 for the SR-20. Also the tail volume coefficient $\bar{V}_h$ is given as $(S_{ref.T}\tilde{l})/(S_{ref}\bar{c})$ where $S_{ref.T}$ is the horizontal stabilizer area and $\tilde{l}$ is the distance measured from the fuselage/wing aerodynamic center and horizontal stabilizer center

of lift. $\bar{V}_h$ for the SR-20 is approximately 0.629. Additionally, the Oswald efficiency factor, e, is estimated empirically as 0.83 based on course materials from aircraft performance course notes at WMU [62]. Finally the cruise condition lift and drag coefficients are given as $C_{L_0} = 0.393$ and $C_{D_0} = 0.019$.

Stability and control derivatives specific to an airframe are obtained though high-level aerodynamic analysis or flight test validations and are often considered proprietary data and held by an aircraft manufacturers. However, empirical and analytical methods to estimate these stability derivatives are widely available and are utilized herein for the Cirrus SR-20. Many of the values estimated for the SR-20 are from relationships given in Etkin [44] and Nelson [60]. For example, C_{L_α} is estimated from Etkin to be 5.24 per radian based on the finite wing lift-curve slope, physical dimensions of the aircraft, typical flight service conditions, and airfoil properties. These texts in addition to course materials for AE3800 and AE4600 [62, 63] provide $C_{M_0} = 0.058$, $C_{M_\alpha} = -1.5$ and $C_{L_{\alpha.T}} = 4.37$ rad^{-1}, and the elevator effectiveness as $a_e = 4.301$ per radian.

Next, calculations and results for the remaining aircraft stability and control variables necessary for the 3-DOF model are provided by [42, 43, 47, 60] in (2.34) to (2.39)

$$C_{L_{\delta_E}} = a_e \frac{S_{ref.T}}{S_{ref}} \tag{2.34}$$

$$C_{L_{\dot{\alpha}}} = 2.2\bar{V}_h \varepsilon_\alpha C_{L_{\alpha.T}} \tag{2.35}$$

$$C_{L_q} = 2.2\bar{V}_h \frac{\tilde{l}}{\bar{c}} C_{L_{\alpha.T}} \tag{2.36}$$

$$C_{M_{\delta_E}} = -a_e \bar{V}_h + 0.0507 C_{L_{\delta_E}} \tag{2.37}$$

$$C_{M_\alpha} = 2.2\bar{V}_h \frac{\tilde{l}}{\bar{c}} \varepsilon_\alpha C_{L_{\alpha.T}} \tag{2.38}$$

$$C_{M_q} - 2.2\bar{V}_h \frac{\tilde{l}}{\bar{c}} C_{L_{\alpha.T}} \tag{2.39}$$

The calculations are summarized in Table 2.2 which provides the approximate 3-DOF aerodynamic model of the Cirrus SR-20. Note that $*$ represents a dimensional stability/control derivative.

Further derived from aircraft performance concepts, the power required curve is given in Figure 2.7 for steady-level flight conditions in which $L = W$ and $T = D$. Therefore the thrust

Table 2.2: Cirrus SR-20 Aircraft Model

Variable	Value	Variable	Value
$\bar{c}$	1.23 m	C_{L_0}	0.393
W	13.3 kN	C_{L_α}	5.24 *
S_{ref}	12.67 m^2	$C_{L_{\delta_E}}$	0.876 *
b	10.7 m	$C_{L_{\dot{\alpha}}}$	2.032 *
e	0.83	C_{L_q}	6.05 *
J_{yy}	2102 kg·m^2	C_{M_0}	0.058
AR	9.05	C_{M_α}	-1.50 *
η_{Prop}	0.85	$C_{M_{\delta_E}}$	-2.66 *
D_{Prop}	1.85 m	$C_{M_{\dot{\alpha}}}$	-6.28 *
C_{D_0}	0.019	C_{M_q}	-18.7 *

required to maintain flight at a given velocity is equal to the total drag force at that flight condition. The plot in Figure 2.7 is obtained from AE3800 course sources and is used to compare the known power required function to forthcoming simulation results. Note that the power available from the SR-20 powerplant is 150kW (200hp) at sea level, which is constant with velocity and when power required and power available intersect, the result is the maximum attainable speed of the aircraft; roughly 100 m/s.

2.5 Propeller Modeling for Thrust

The SR-20 is equipped a constant-speed propeller (CSP). In contrast to a fixed-pitch propeller, a CSP permits a maximum η_{Prop} based on P_{ps} and flight condition. This is accomplished through a passive control system in the propeller hub which automatically adjusts the propeller blade angle, $\theta_{P_{3/4}}$, where $3/4$ represents the blade angle at 3/4 the propeller radius, by means of a flyweight and an engine oil pump to actuate the hub pitch mechanism. This is analogous to an automatic transmission in a road vehicle which shifts gears to avoid over-speeding the engine and allowing for higher efficiency though varying speeds.

Several metrics are needed to quantify the propeller model developed for the SR-20 CSP.

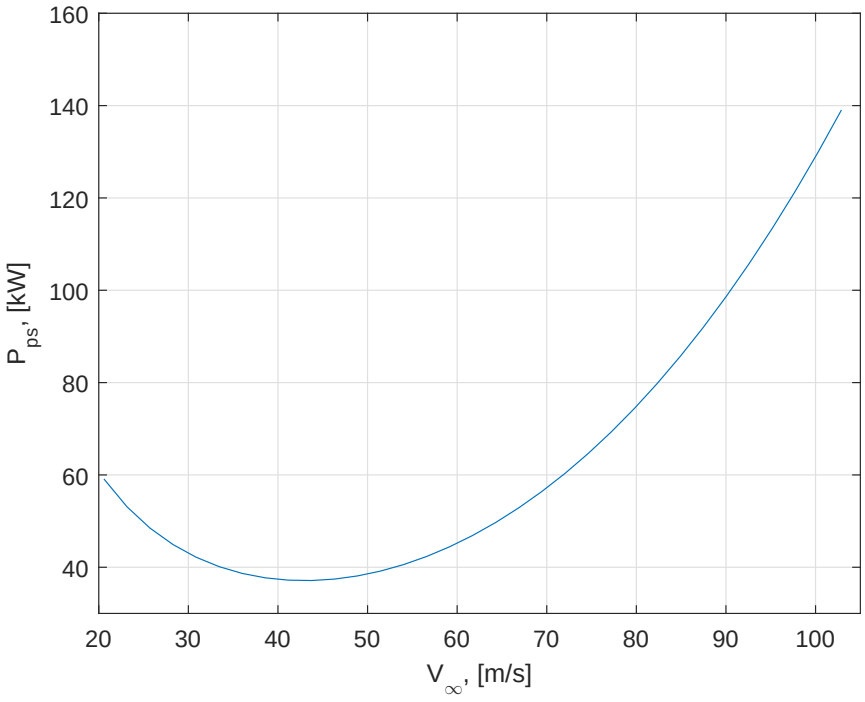

Figure 2.7: Power output requirement for steady-level flight for the SR-20; $T = D$ [62]

The advance ratio, ξ, and power coefficient, C_p, are provided in (2.40) and (2.41), respectively,

$$\xi = \frac{V_\infty}{\underset{\sim}{\omega}_{Prop} D_{Prop}} \tag{2.40}$$

$$C_p = \frac{P_{ps}}{\rho_\infty \underset{\sim}{\omega}^3_{Prop} D^5_{Prop}} \tag{2.41}$$

where $\underset{\sim}{\omega}_{Prop}$ is the propeller angular velocity measured in revolutions per second and the value of ρ_∞ is taken at sea level, and D_{Prop} is the propeller diameter [67]. While an individual propeller can have unique physical and aerodynamic properties, (2.40) and (2.41) apply regardless of the propeller configuration; e.g. fixed-pitch, variable pitch, or CSP.

Modeling of the CSP propeller is accomplished by first taking (2.40) and developing an appropriate range of ξ for the aircraft and propeller limits as established by the FAA in the TCDS for the Cirrus SR-20 [64, 67]. Figure 2.8 illustrates that η_{Prop} is a function of ξ and $\theta_{P_{3/4}}$. Note that a CSP obtains the maximum η_{Prop} by varying $\theta_{P_{3/4}}$. Based on the propeller and SR-20 limitations set by the FAA, $\xi \in [0.75\ 1.64]$. This set also corresponds closely to Figure 2.8 which is a generalized propeller efficiency plot.

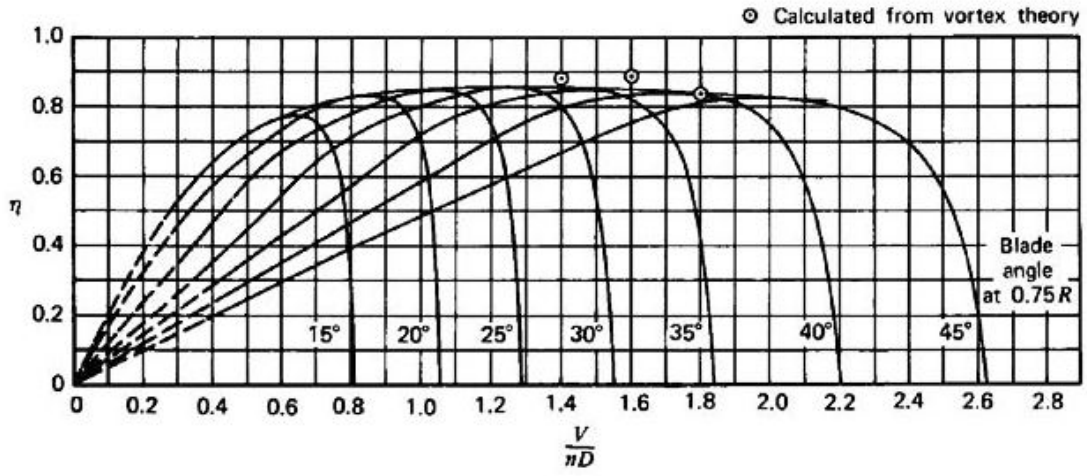

Figure 2.8: Generalized η_{Prop} as function of ξ and $\theta_{P_{3/4}}$ for a 3-bladed propeller; reproduced from [46]

Further, C_p and ξ can be related by data given in the *Generalized Method of Propeller Performance Estimation* [68]. Appropriate design parameters of the propeller, such as the activity factor and design lift coefficient, have large effects on the relationship between C_p and ξ. Therefore, the activity factor and design lift coefficient values are chosen such that there is an acceptable correlation between the calculated C_p and ξ from [68] and flight test data from the SR-20. A sample of the selected propeller model is given in Figure 2.9. By locating η_{Prop} of 0.85 and bounding ξ by $\theta_{P_{3/4}}$ limits for the SR-20, C_p and ξ can be described by the linear fit based on the data in Figure 2.9 in the form given in (2.42).

$$C_p = m\xi + b = 0.1228\xi - 0.0473 \tag{2.42}$$

which results in an R^2 of 0.994. The selected propeller activity factor and design lift coefficient is 80 and 0.15, respectively.

Next, (2.41) is restated by substituting the linear curve fit in (2.42) and solving for P_{ps}. Thus, P_{ps} is now a function of V_∞ and ω_{Prop} as given in (2.43), which is unique to the propeller

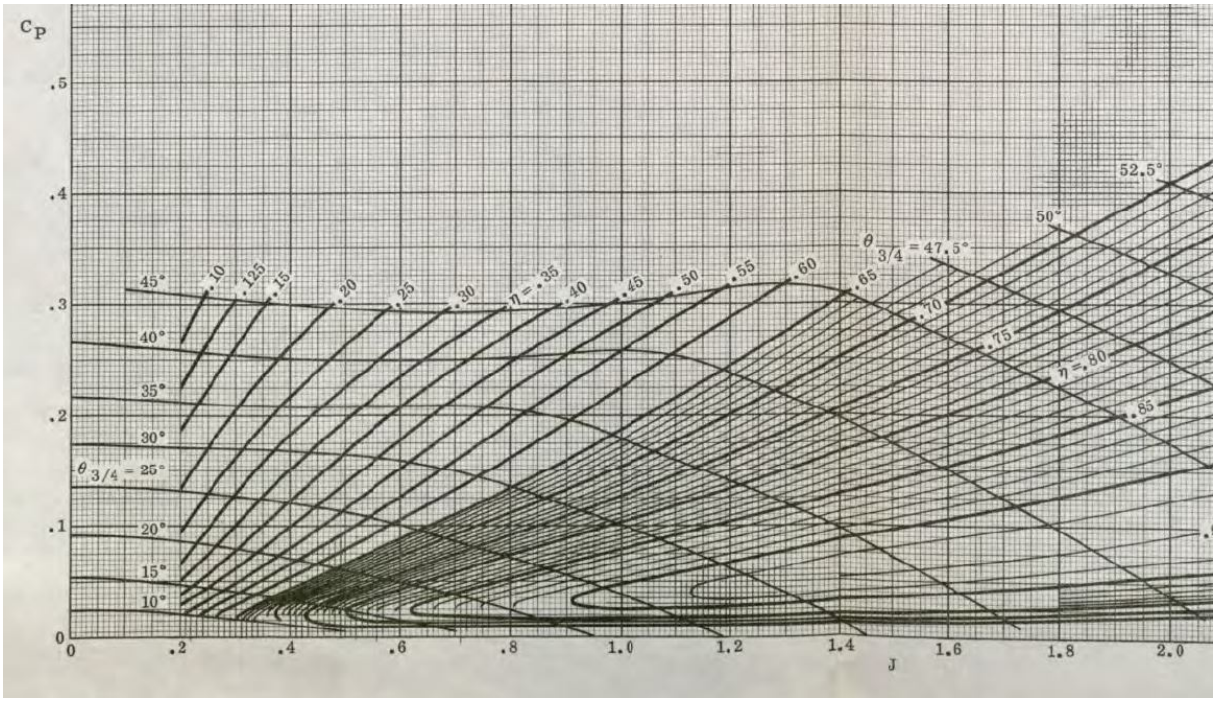

Figure 2.9: C_p as a function of ξ and η_{Prop}; reproduced from [68] where J=ξ

characteristics given which approximate the performance observed in flight test data.

$$
\begin{aligned}
P_{ps} &= C_p(\xi)\rho_\infty \underset{\sim}{\omega}^3_{Prop} D^5_{Prop} \\
P_{ps} &= (0.1228\frac{V_\infty}{\underset{\sim}{\omega}_{Prop} D_{Prop}} - 0.0473)\rho_\infty \underset{\sim}{\omega}^3_{Prop} D^5_{Prop} \\
P_{ps} &= 1.173(V_\infty - 0.713\underset{\sim}{\omega}_{Prop})\underset{\sim}{\omega}^2_{Prop}
\end{aligned}
\tag{2.43}
$$

For the typical range of ω_{Prop} and V_∞ seen by the CSP serving as the domain of (2.43), P_{ps} is plotted in Figure 2.10 using normalized values for the respective variables in the model. Several observations become apparent. First, for the FAA acceptable flight ranges V_∞ and ω_{Prop} for the SR-20, there is a band of permissible P_{ps}. This signifies that certain combinations of V_∞ and ω_{Prop} violate the CSP model as η_{Prop}, ξ, and $\theta_{P_{3/4}}$ limits are integrated into (2.43) by the modeling approach in the section. Second, by inspection, the data set agrees with propeller and aircraft dynamics fundamentals; that is, by Figure 2.10, low P_{ps} values cannot yield high V_∞ values. Further, for higher P_{ps}, a wide range of V_∞ is available, compared to the lower P_{ps} region. This propeller model is used in order to relate the HEP shaft power to aircraft velocity so that the

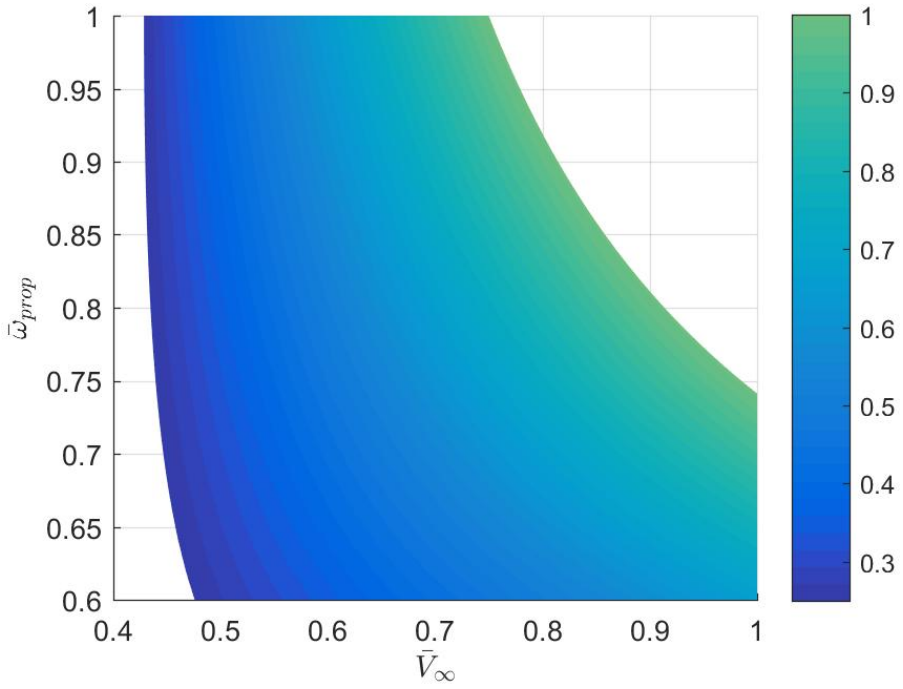

Figure 2.10: The CSP propeller model for the SR-20; color scale represents $\bar{P}_{ps}$

ICE and ED angular velocities can be calculated which satisfy the propulsion system demands to achieve a desired aircraft velocity and altitude, and therefore, propulsive thrust.

2.6 Power and State Interconnections

To complete the system model, interconnections between components are needed. Recall that the HEP system herein is a switched mode system: (i) battery discharging and ED propelling and (ii) battery charging and ED generating. Therefore, each mode has unique power flow directions which must be reflected in the interconnection constraints between components. The ICE, ED, battery, mechanical and electrical bus, aircraft, and propeller interconnections are, for both modes:

$$\bar{P}_{ps} = \bar{P}_{ps}(\bar{V}_\infty, \bar{\omega}_{Prop}) \tag{2.44}$$

$$\bar{P}_{ICE}^{fuel} = \bar{P}_{ICE}^{fuel}(\bar{\omega}_{ICE}, \delta_T) \tag{2.45}$$

$$\bar{P}_{ICE}^{out} = \bar{P}_{ICE}^{out}(\bar{\omega}_{ICE}, \delta_T) \tag{2.46}$$

unique to mode 1 :

$$P^1_{ED,M} = \eta^p_{ED}\eta^p_{Inv}P^1_{ED,E} \tag{2.47}$$

$$P^1_{ED,E} = P^{MAX,g}_{ED,E}u^1_{ED} \tag{2.48}$$

$$\eta_{DCC}P^1_{Bat} = P^1_{ED,E} \tag{2.49}$$

$$P^1_{HEP} = \eta_{CVT}P^{out}_{ICE} + P^1_{ED,M} \tag{2.50}$$

and unique to mode 2:

$$P^2_{ED,M} = P^{MAX,g}_{ED,m}u^2_{ED} \tag{2.51}$$

$$P^2_{ED,E} = \eta^g_{ED}\eta^g_{Inv}P^2_{ED,M} \tag{2.52}$$

$$P^2_{Bat} = -P^2_{ED,E}/\eta_{DCC} \tag{2.53}$$

$$P^2_{HEP} = \eta_{CVT}P^{out}_{ICE} - P^2_{ED,M} \tag{2.54}$$

CHAPTER 3

MODEL PREDICTIVE CONTROL BACKGROUND AND IMPLEMENTATION

3.1 Introduction

Model Predictive Control (MPC) is utilized to solve to solve the forthcoming control problem because it offers advantages that classical controls do not. For example, PID control, does not explicitly consider the future impact of current control actions [69]. MPC first appeared in late seventies and has seen wide use across disciplines [70]. MPC is an optimization-based method to determine the control inputs to a dynamic system based upon choosing control inputs to be applied from current time to a future time. Specifically, the system trajectories are predicted into the future from the current time point with control inputs chosen to minimize some objective function while satisfying state, algebraic, and control variable constraints. MPC can be used with a large variety of applications, but is best for linear and/or nonlinear problems in which there are a large number of manipulated and controlled variables and those variable's respective constraints and changing control objectives [71]. Note that MPC does not represent one specific control strategy, but rather offers a range of control methods to make use of a model to output a control signal by means of the objective function previously mentioned. The main concepts of a MPC approach are:

- Use of a linear, or nonlinear, model to predict the plant output at some future time (horizon).
- The horizon is moved towards the future so that the control signals for each partition are calculated within each time step.
- Calculation of a control input vector which minimizes an objective function which usually contains terms that describe reference tracking error, use of resources, or change in control inputs over time.

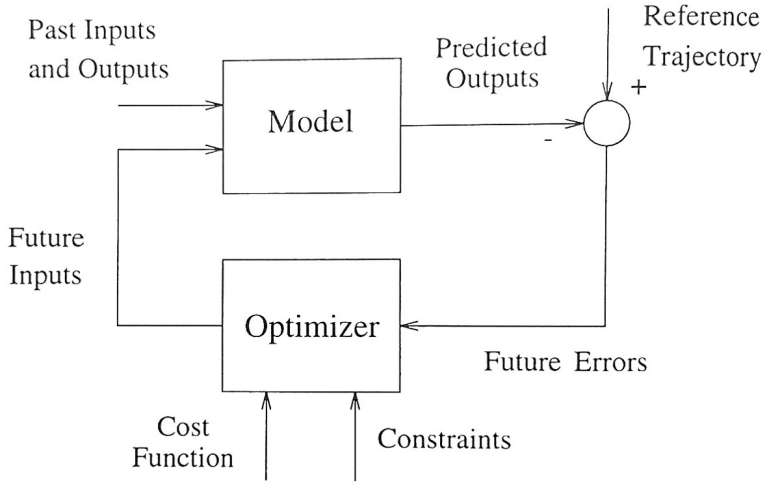

Figure 3.1: Block diagram structure of an MPC problem; reproduced from [70]

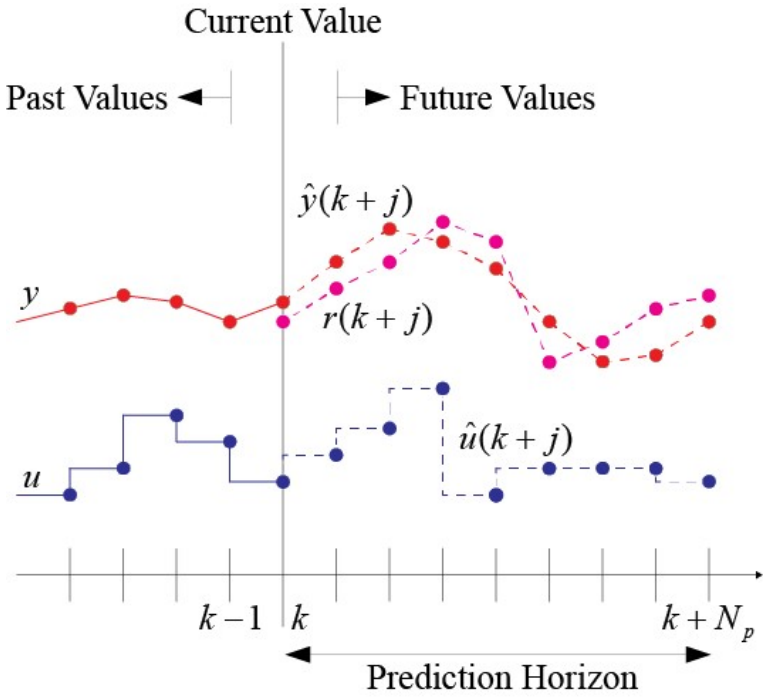

Figure 3.2: Model predictive control example

The structure of an MPC control problem is presented in Figure 3.1 [70]. The two primary components unique to MPC are the optimizer and the model. The model plays an important part in the simulation as it is required to predict future states as a result of control inputs from the optimizer. It is necessary for the model to capture all necessary dynamics within a horizon so that no important information regarding the model is neglected. The optimizer minimizes the

(usually) quadratic control problem objective function. When equality or inequality constraints are introduced, the complexity and computational expensive operations increase. The number of variables in the optimization also leads to increased computational time. All other components shown in Figure 3.1 are apparent. The strategy in which the MPC is implemented is provided in the next section.

3.1.1 Methodology

An MPC control problem, is stated in (3.1) through (3.4).

$$\min_{u} \{J = \int_{t_0}^{t_f} f(t,x,y,u,r)dt\} \tag{3.1}$$

subject to:

$$\frac{dx}{dt} = g_x(t,x,y,u) \tag{3.2}$$

$$g_y(t,x,y,u) = 0 \tag{3.3}$$

$$h(t,x,y,u) \leq 0 \tag{3.4}$$

where t_0 is the current time; t_f is the future time; the difference between future and current time $(t_f - t_0)$ is called the prediction horizon, T_w; x is the system state vector; y is a vector of algebraic variables that includes connection variables and/or output variables; u is the vector of control inputs; r are reference values to track; J is the objective function (or performance index) to be minimized over the prediction horizon with choice of u ; $g_x(\cdot)$ is the dynamical vector field; $g_y(\cdot)$ are the algebraic variable equality constraints; $h(\cdot)$ describes the inequality constraints. Figure 3.2 provides a visualization of how MPC is executed. Over the prediction horizon, the system dynamics and constraints are evaluated and satisfied. T_w is divided into an integer number of partitions N_p.

A variety of methods are available to discretize MPC control problem dynamics. Collocation, [72], forward-, backward-, or central-difference dicritizeations methods are often used. Further, the objective function integral is approximated using trapezoidal numerical integration.

After dicritizeation, the MPC methodology given in (3.1) through (3.4) is now:

$$\min_{U} \sum_{j=0}^{N_p} f_j(t(k+j), \hat{x}(k+j), \hat{y}(k+j), \hat{u}(k+j), \hat{r}(k+j)) \tag{3.5}$$

subject to:

$$g_y^d(t, x(k), X, y(k), Y, u(k), U) = 0 \tag{3.6}$$

$$h^d(t, x(k), X, y(k), Y, u(k), U) \leq 0 \tag{3.7}$$

$$\hat{x}(k+1) = g_x^d(t(k), x(k), \hat{x}(k+1), y(k), \hat{y}(k+1), \hat{u}(k+1)) \tag{3.8}$$

$$\hat{x}(k+2) = g_x^d(t(k+1), \hat{x}(k+1), \hat{x}(k+2), \hat{y}(k+1), \hat{y}(k+2), \hat{u}(k+2))$$

$$\vdots$$

$$\hat{x}(k+N_p) = g_x^d(t(k+N_p-1), \hat{x}(k+N_p-1), \hat{x}(k+N_p), \hat{y}(k+N_p-1), \hat{y}(k+N_p), \hat{u}(k+N_p)$$

where k is an integer-valued index for some regularly spaced time vector with increment $h = T_w/N_p$, $\hat{x}$ is the estimate of the state value from the discretized system based on system information at k and selected control inputs, $\hat{y}$ is the estimate of the algebraic variables, $\hat{u}$ are the predicted control inputs, $U = [\hat{u}(k+1), ..., \hat{u}(k+N_p)]^T$, $X = [\hat{x}(k+1), ..., \hat{x}(k+N_p)]^T$, $Y = [\hat{y}(k+1), ..., \hat{y}(k+N_p)]^T$, and g_x^d , g_y^d , h^d are the result of discritizing $g_x(\cdot)$, $g_y(\cdot)$, and $h(\cdot)$, respectively. Note that the control inputs are referenced starting at $k+1$ and do not start at k. This is because the control inputs are piece-wise constant and are applied over the interval $(k+j, k+j-1]$. Thus the move from $x(k+j)$ to $x(k+j+1)$ is driven by the control over $(k+j, k+j-1]$ which is not applied until $k+\varepsilon$ for $\varepsilon << 1$, but remains constant through $k+j+1$.

Now, the MP control problem can be solved using the approach presented in the following steps:

1. Initial conditions provided at $k = 0$; x_0 and u_0.

2. Solve MPCDCP over $(t_0, t_f]$ for $t_o = k \cdot h$ and $t_f = (k \cdot N_p)h$ with an optimizer (sequential quadratic programming for example) so that the control inputs minimize the objective function J, which outputs U^*; the optimized discritized control input.

3. Simulate the nonlinear system from t_0 to $t_0 + h$ with the control input equal to $u(k+1) = \hat{u}^*(k+1)$ using a numerical differential equation solver. The output of the solver serves as

the starting state values for the run of the optimizer in the coming horizon.

4. If $t_0 + h$ is not equal to the overall simulation end time, T_f, increment the current time by h, $k = k + 1$ and return to step (2). Otherwise, simulation is complete and shrink horizon window as t approaches T_f.

3.2 Supervisory Level System Model

The HEP system herein is capable of operating in one of two modes that has a unique power flow direction configuration. Specifically, in mode 1 the ED is propelling and the battery is discharging and in mode 2 the ED is generating and the battery is charging. Each mode has a unique set of dynamics and algebraic functions that describe the power flow. The mode control vector is defined as $\lambda(t) = [\lambda_1(t), \lambda_2(t)]^\top$ where $\lambda_i(t) \in \{0, 1\}$ and

$$\lambda_1(t) + \lambda_2(t) = 1, \tag{3.9}$$

to ensure that only one mode is active at a time; when $\lambda_1(t) = 1$, mode 1 is on and when $\lambda_2(t) = 1$, mode 2 is on.

3.2.1 System Dynamics

Each λ_i has its own set of operating dynamics that produces outputs specific to that mode. The state dynamics for the switched system is the mode-switched combination of the dynamics

$$\dot{x} = \lambda_1 f_1(x, y^1, u^1) + \lambda_2 f_2(x, y^2, u^2) \tag{3.10}$$

where f_i is the mode i dynamical vector fields, x is the state vector

$$x = [V_\infty, \alpha, \theta, q, \chi, \hbar, R_{CVT}, \delta_T, \overline{W}_{Bat}, \omega_{Prop}]^\top, \tag{3.11}$$

and u^i and y^i, $i = 1,2$, are the mode specific control inputs and algebraic variables which are functions of the states and mode specific control inputs.

$$u^i = [u^i_{\delta_E}, u^i_{CVT}, u^i_{\delta_T}, u^i_{ED}]^\top \tag{3.12}$$

$$y^i = [P^{fuel^i}_{ICE} P^{out^i}_{ICE}, P^i_{ED,M}, P^i_{ED,E}, P^i_{Bat}, P^i_{HEP}]^\top \tag{3.13}$$

Optimal power management in the HEP system is desired and is the control problem to be solved. This is achieved by the minimization of a integral quadratic performance index (PI), denoted J, based on desired altitude, speed, fuel economy, and battery charge:

$$\min_{u^1,u^2,\lambda} J(x_0, t_{p,0}, t_{p,f}, u^1, u^2, \lambda) \tag{3.14}$$

subject to the system component constraints and the PI is given as:

$$\begin{aligned} J = &\int_{t_{p,0}}^{t_{p,f}} \mu_{V_\infty} \left(\frac{V_\infty(t) - V_{ref}}{V^P_{ref}} \right)^2 dt + \int_{t_{p,0}}^{t_{p,f}} \mu_{\hbar} \left(\frac{\hbar(t) - \hbar_{ref}}{\hbar^P_{ref}} \right)^2 dt + \int_{t_{p,0}}^{t_{p,f}} \mu_{Bat} (\overline{W}_{Bat} - \overline{W}_{Bat,des})^2 dt \\ &+ \int_{t_{p,0}}^{t_{p,f}} \mu_{P^{fuel}_{ICE}} \left(\frac{P^{fuel}_{ICE}(t)}{P^{fuel_{MAX}}_{ICE}} \right)^2 dt \end{aligned} \tag{3.15}$$

where μ_{V_∞}, $\mu_{\hbar}$, μ_{Bat}, and $\mu_{P^{fuel}_{ICE}}$ as the penalty weights on velocity tracking error, altitude tracking error, battery state of charge deviation, and fuel usage, respectively over the partition time span $t_{p,0}$ to $t_{p,f}$. V^P_{ref} and $\hbar^P_{ref}$ are the maximum trajectory (velocity, altitude) values over the prediction horizon and are used as normalization factors to promote solution convergence. Note that fuel power is chosen to be minimized rather fuel use in mass because the latter is proportional to the former, thus minimizing fuel power minimizes fuel usage.

3.2.2 Switched Optimal Control Problem

To solve the preceding switched optimal control problem (SOCP) normally requires mixed-integer programming or similar methods. An alternative solution method is the embedding method, which has been shown to result in faster, lower PI valued solutions in a majority of situations [73].

The embedding method recasts the discrete-valued mode switches onto continuous-valued ones $\tilde{\lambda}_i \in [0,1]$ (the embedded mode switches), resulting in a continuous-valued problem. The embedded optimal control problem (EOCP) is solvable using traditional numerical approaches such as sequential quadratic programming. This transformation allows for solving of the switched hybrid optimal control problem in software functions such as MATLAB's $fmincon()$. Rather than $\lambda_i \in \{0,1\}$, the switched model allows for each λ_i to take on real numbers in the closed interval $[0,1]$; also stated as, $\tilde{\lambda}(t) \in [0,1] \times [0,1]$; with the equality constraint $\tilde{\lambda}_1 + \tilde{\lambda}_2 = 1$. The EOCP here meets the sufficient conditions [74, 75] necessary for the existence of a global (possibly non-unique) minimum: the dynamical system equations are linear in the continuous control inputs and the objective function is quadratic in the continuous control inputs. Further, the trajectories of the SOCP are dense in those of the EOCP. This means that either the EOCP solution contains an optimal SOCP solution or that an SOCP solution can be constructed that approximates the EOCP optimal solution to an arbitrary degree. Note that state, control inputs, and algebraic variables associated with the EOCP problem are denoted with $\tilde{(\cdot)}$.

3.2.3 Mode and Control Projection

If $\tilde{\lambda}_i^* \in \{0,1\}$ over the prediction horizon except for time intervals of zero measure, then the EOCP solution is an SOCP solution; otherwise an approximating SOCP solution must be constructed that determines both the mode and continuous control inputs to apply, termed mode and control projection. In order to approximate the optimal EOCP solution here, the largest embedded mode value is projected to one in order to set the active mode. Meyer et al. [34] proposes the mode projection algorithm as

$$K = \underset{i \in \{1,2\}}{\operatorname{argmax}} \ \tilde{\lambda}_i^* \tag{3.16}$$

where K is the projected active mode, which results in $\tilde{\lambda}_K = 1$ and $\lambda_i = 0, \forall i \neq K$. However, if the embedded mode switch values are equal, the mode is not changed from the previous value. Further, the continuous control applied to the switched system is chosen to be equal to the embedded control, i.e., $u^K = \tilde{\lambda}\tilde{u}^{K,*}$.

CHAPTER 4

SIMULATION OF A HYBRID CIRRUS SR-20

MPC is implemented in the switched mode HEP system with the models and strategy defined thus far. Simulations are performed in MATLAB over a variety of flight scenarios and test cases to validate the HEP system operation. The HEP Cirrus SR-20, denoted as SR-20h, will be used throughout this section to denote the hybrid aircraft in comparison to the standard SR-20. For all the simulations herein, the continuous-time aircraft HEP system is discretized using collocation [76] and the PI from (3.15) is approximated using trapezoidal numerical integration for the state variables and rectangular numerical integration for terms with algebraic power, mode switch, and control input variables. The prediction horizon for the MPC simulation is set to 2 s and divided into two 1 s partitions and the continuous and discrete-valued control inputs are constant within a partition.

For a valid comparison between the the hybrid and non hybrid SR-20, as well as from a certification and safety standpoint, the components, weight and balance, and performance of the SR-20h is kept as similar as possible to the SR-20. The SR-20 comes equipped with an Continental IO-360ES ICE which can deliver 157 kW in steady state at 294 rad/s [65]. The IO-360ES weights 320 pounds as shipped from the manufacturer. An additional 20% of the dry weight is assumed for accessories, engine mounts, and oil resulting in the installed SR-20 powerplant weighing roughly 384 pounds. The SR-20h propulsion system consists of the ROTAX 912iSc Sport which weighs 166 pounds including all accessories [55]. Also the UQM PowerPhase 100 and inverter weigh 110 and 61 pounds respectively. The CVT and other associated HEP powertrain components are assumed to add 20% of the ICE and ED combined weight giving the HEP powertrain total weight, excluding batteries, to be 404 pounds; only 5% more weight than the SR-20 for nearly the same maximum output power. Additionally, the HEP components are sized to fit within the engine bay occupied by the IO-360ES; considerations for installation and component orientation are beyond

the scope of this work.

Fuel for the SR-20 is carried in the wings and due to the introduction of the HEP system, some of the fuel volume is replaced by batteries. The SR-20 TCDS [64] specifies the total fuel volume of the SR 20 as 60.5 gallons, equivalent to 388 pounds when using 6.07 lb/gal as the fuel density. One battery pack, which contains 27 Saft 12Ah modules, weights 66 pounds, displacing approximately 11 gallons of fuel. Three battery packs are selected for the SR-20h, weighing 198 pounds which leaves 190 pounds of fuel equal to 31 gallons. The battery packs are assumed to be located in the void left by the volume of the fuel removed, in the cargo compartment, or other location in order to satisfy the weight and balance envelope of the SR-20.

4.1 Validation Simulation Over a Prescribed Flight Profile

The first HEP simulation is performed to validate the expected HEP system model and aircraft response. This is accomplished by generating a flight profile which consists of climb, descent, steep climb, and steady-level flight segments. Specific to this validation profile, the PI penalties are $\mu_{V_\infty} = 500$, $\mu_{\hbar} = 3000$, $\mu_{P_{ICE}^{fuel}} = 0$ and μ_{Bat} has the form given in (4.1):

$$\mu_{Bat} = \begin{cases} 0, & \Delta\overline{W}_{Bat}(t_{p,0}) \geq 0 \\ 500(1+20|\overline{W}_{Bat}(t_{p,0})|), & \Delta\overline{W}_{Bat}(t_{p,0}) < 0 \end{cases} \tag{4.1}$$

where $\Delta\overline{W}_{Bat}(t_{p,0}) = W_{Bat}(t_{p,0}) - \overline{W}_{Bat,des}$ and $\overline{W}_{Bat,des}$ is the desired state of charge of 0.6. Therefore, (4.1) yields an increased penalty on the battery state of charge deviation as it falls further from a desired value, minimally penalizes battery discharge (end ED use) when the battery is near the desired charge values, and does not penalize overcharging the battery so as to capture excess energy for later use. This same approach is applied in the other simulations, but contain different formulations of μ_{Bat} to achieve desired simulation performance.

The aircraft response given the simulation conditions and system model definitions is demonstrated in Figure 4.1 where the 2-norm normalized error for velocity and altitude tracking are 0.19% and 0.04%, respectively. The 2-norm normalized error quantifies how well the simulation trajectory adheres to the desired trajectory whose general form is given in (4.2) for any

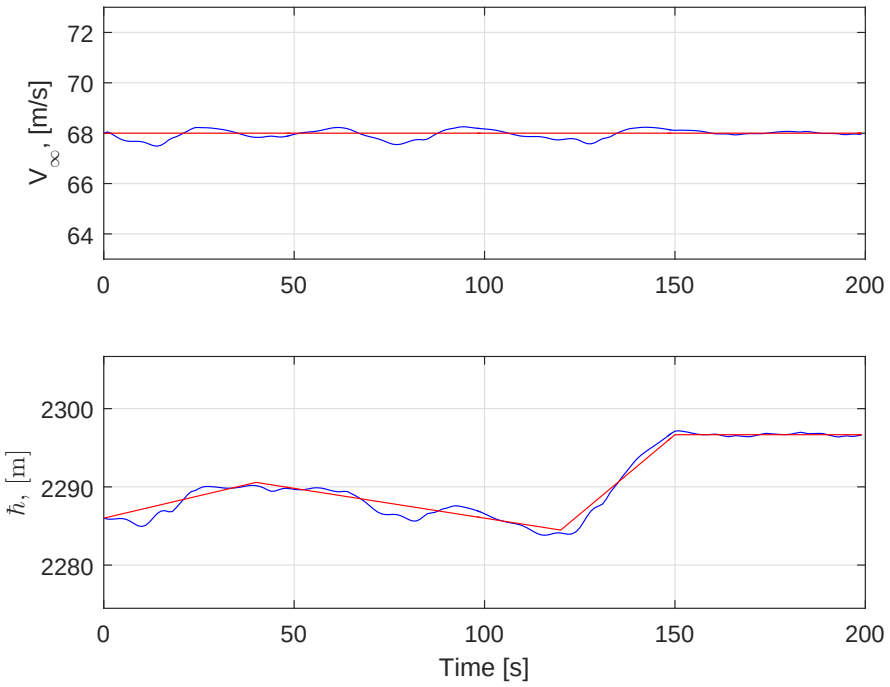

Figure 4.1: Simulated V_∞ and $\hbar$ over the Validation flight profile: (—) simulated trajectory, (—) desired trajectory.

variable κ which has simulated and desired values at each point in the simulation, i, over the total number of simulation points, N.

$$||\kappa||_2 = \frac{\sqrt{\sum_{i=1}^{N}(\kappa_{sim}^i - \kappa_{des}^i)}}{\sqrt{\sum_{i=1}^{N}\kappa_{des}^i}} \tag{4.2}$$

Further, Figure 4.2 provides the HEP power output to the propeller via the mechanical bus operation given in Figure 4.3. Note that when in the steady-level flight phase from 150 s onward, P_{HEP} is roughly 70 kW, which is approximately equal to the expected steady power required shown in Figure 2.7 at the flight velocity given in this simulation, which provides another validation of the aircraft dynamics and HEP system.

One of the main purposes of a HEP system is to promote fuel efficiency. The impact of $\mu_{P_{ICE}^{fuel}}$ on fuel use is examined which provides insight into the ability of the HEP system to minimize fuel consumption. This simulation increases $\mu_{P_{ICE}^{fuel}}$ from 0 to 0.001 while μ_{V_∞} and $\mu_\hbar$ are held at the same values. Figures 4.4 and Figure 4.5 give the ROTAX 912iSc Sport operating

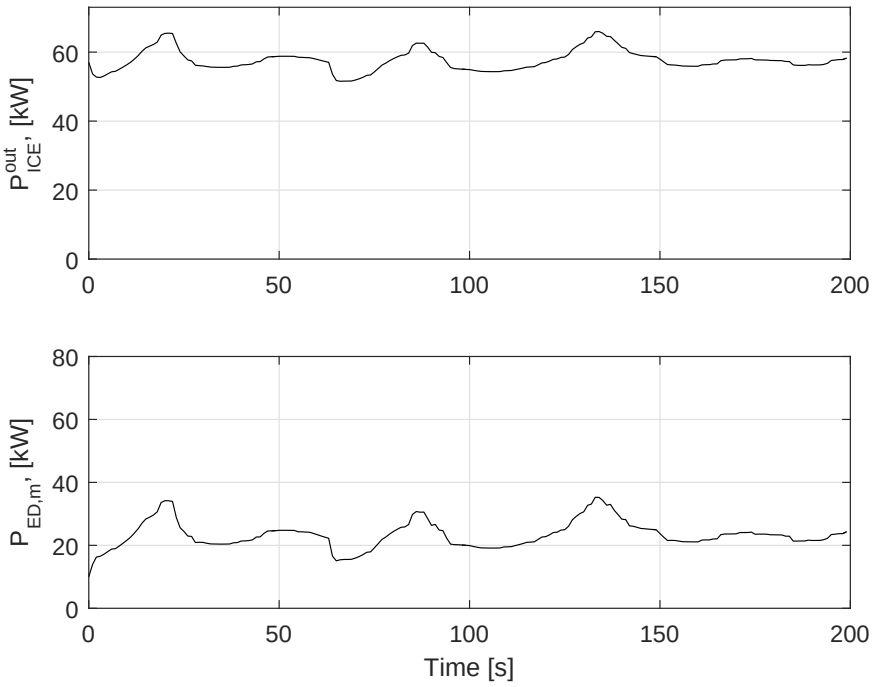

Figure 4.2: Validation profile HEP power from the ICE and ED

points unique to this simulation which display the effect of the fuel penalty in which the fuel penalty simulation indicates operation in more fuel efficient regions. The corresponding HEP system power and mechanical bus dynamics are given in Figure 4.6 and Figure 4.7. When the HEP power and mechanical bus operation is compared to the simulation earlier where $\mu_{P^{fuel}_{ICE}}$ is zero, it is apparent that the HEP component operations are changed in order to provide better fuel efficiency for the given simulation conditions. Between the two models described, a 50% fuel savings was observed for the short profile by increasing the fuel penalty, this value would decrease as propulsion system demands over the flight profile change and for when battery charging is required.

This initial validation profile simulation demonstrates an implementation of MPC for a switched hybrid propulsion system for aircraft. For the μ_i chosen, the simulation provides an optimal model predictive power flow management in the parallel HEP supervisory-level system.

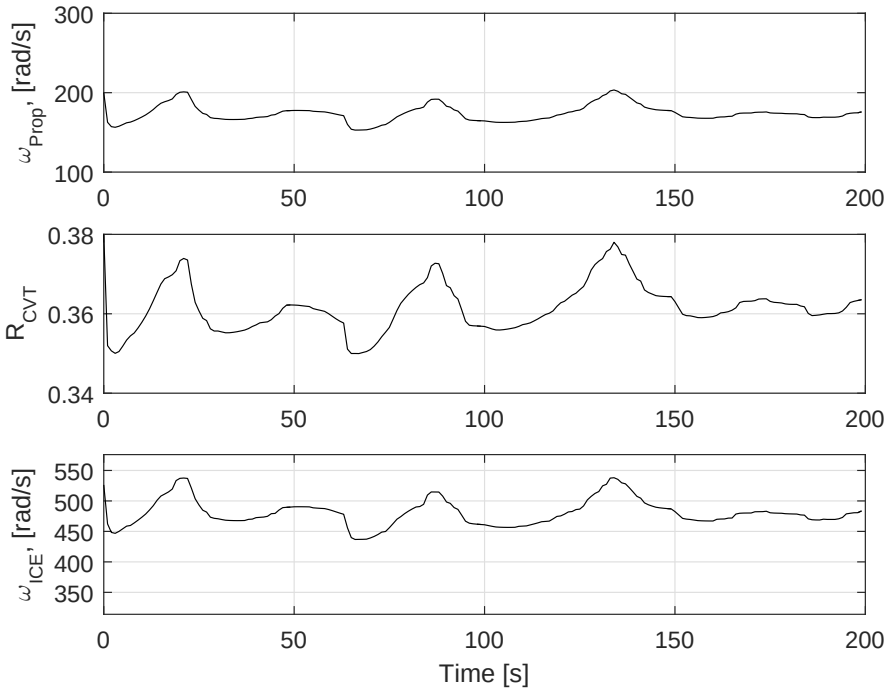

Figure 4.3: Validation profile mechanical bus and ICE operation; propeller speed, CVT gear ratio, and ICE speed (top to bottom)

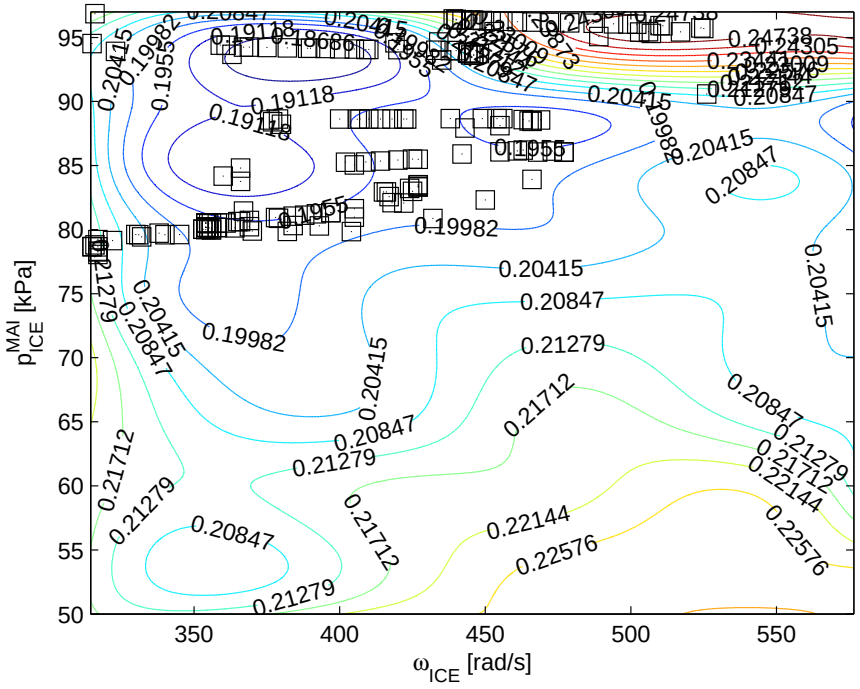

Figure 4.4: ICE operating points on the BSFC map for the Validation flight profile which provides high fuel economy, i.e. increased ED power

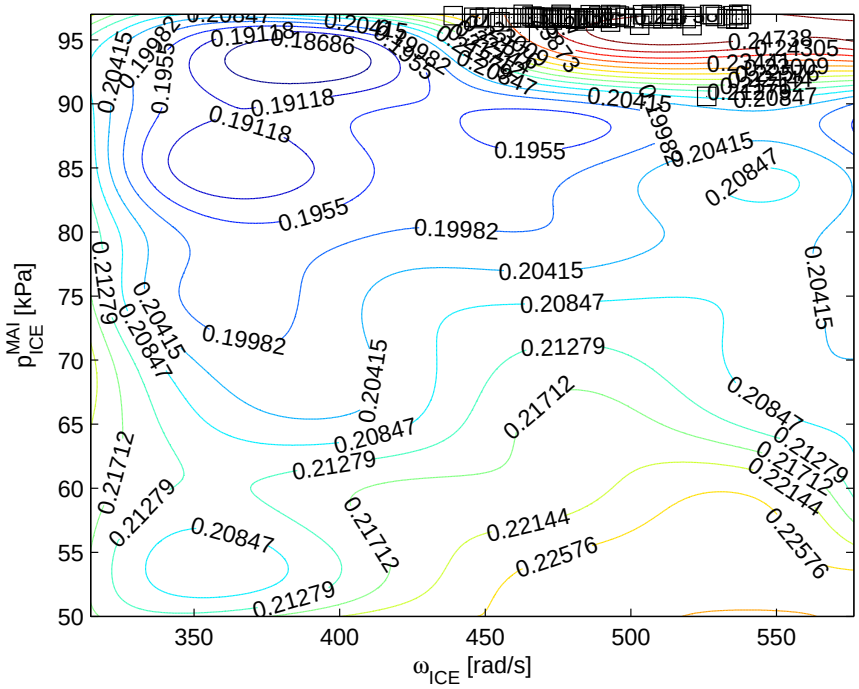

Figure 4.5: ICE operating points on the BSFC map for the Validation flight profile with no fuel economy consideration

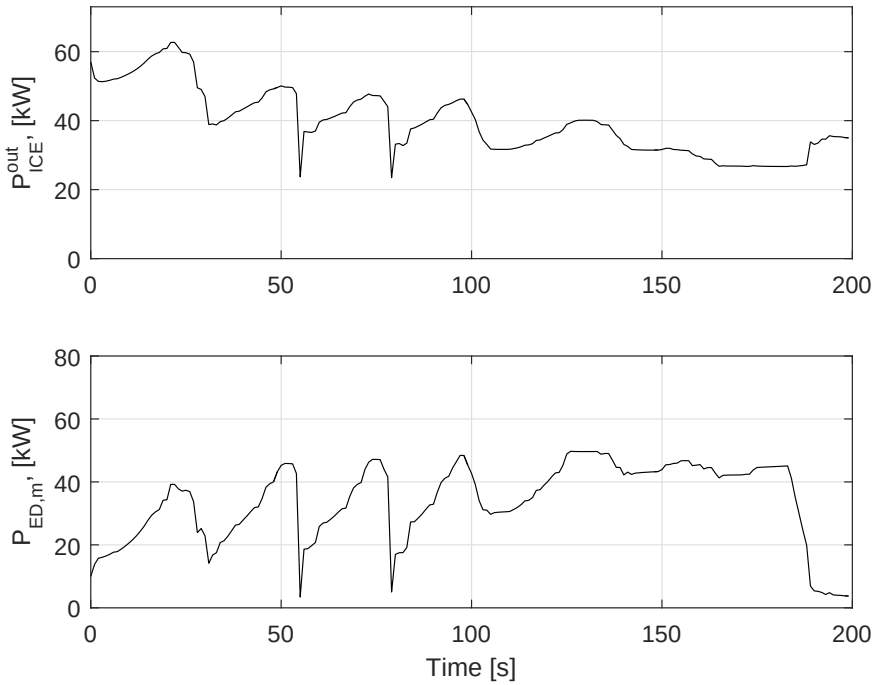

Figure 4.6: Validation profile HEP power from the ICE and ED for $\mu_{P_{ICE}^{fuel}} = 0.001$

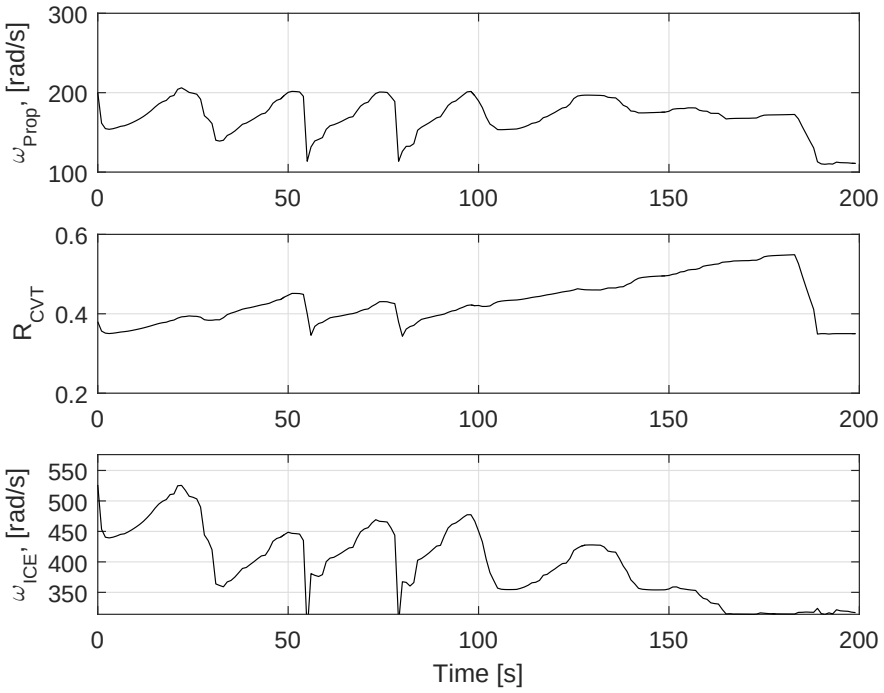

Figure 4.7: Validation profile mechanical bus and ICE operation; propeller speed, CVT gear ratio, and ICE speed (top to bottom) for $\mu_{P_{ICE}^{fuel}} = 0.001$

4.2 Sawtooth Flight Profile Simulation

Another flight profile to test HEP system is in the form of a "sawtooth" profile which consists of climb and descent phases while maintaining a constant velocity. Two situations are considered, one where there is no penalty on fuel usage, and one with a penalty on fuel usage. The PI penalty weights were chosen after numerical testing to achieve acceptable performance from the HEP system: $\mu_{V_\infty} = 100$, $\mu_{\hbar} = 4000$, $\mu_{P_{ICE}^{fuel}}$ is $\in \{0, 1 \times 10^{-3}\}$ and μ_{Bat} is similar to (4.1) where μ_{Bat} for a state-of-charge below the desired level is equal to $50(1 + 20|\overline{W}_{Bat}(t_{p,0})|)$. The large magnitude differences in the μ_i for the sawtooth simulation are a result of how the errors are defined in (3.15). Because altitude and velocity maximum values differ greatly in their relative scale, $\mu_{\hbar}$ must be larger than μ_{V_∞}.

The first set of results provided are for the case where no fuel penalty is given. The SR-20h sawtooth simulation can be seen in Figure 4.8 which shows acceptable tracking where the 2-norm normalized errors for velocity and altitude are calculated to be 0.216%, and 0.03%, respectively.

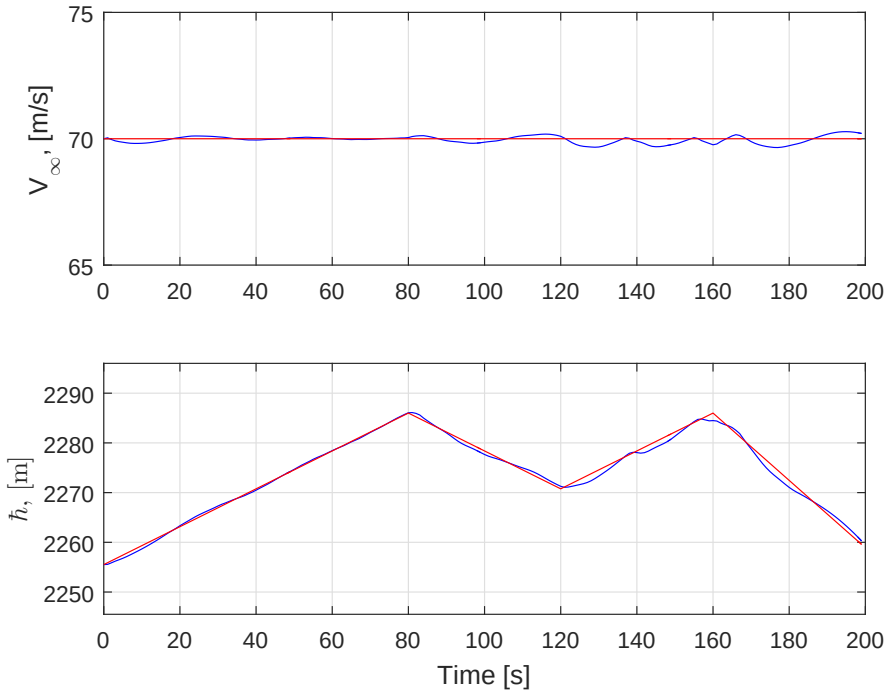

Figure 4.8: Simulated V_∞ and $\hbar$ over the sawtooth profile: (—) simulated trajectory, (—) desired trajectory.

When the profile maximums are reached, oscillations can be observed which indicate the aircraft attempting to regain tracking, i.e., minimize the error in the PI. The simulation of the aircraft trajectory in Figure 4.8 does provide validation again that the MPC implementation of the aircraft dynamics are functional.

Next, when examining the HEP operation over the sawtooth profile, several observations can be made. The mechanical power in the HEP system, for both the ICE and ED, is displayed in Figure 4.9. The ED and ICE powers compliment each other to provide the required power to track the desired altitude and velocity. This shows that the optimizer is allowing the ICE to operate with the ED based on the given dynamics and constraints to achieve the minimization of the PI. The mechanical bus operation is seen in Figure 4.11 which shows the operation of the CVT which connects the ICE and propeller shaft powers and angular velocities all operating within their respective limits. Further, $\overline{W}_{Bat}$ and P_{Bat} are given in Figure 4.10 which demonstrate that the ED inverter and propelling efficiencies are accounted for in the given power demand. Note that when P_{Bat} is large, the change in $\overline{W}_{Bat}$ for a given ΔT is reasonable in that large battery power draw will

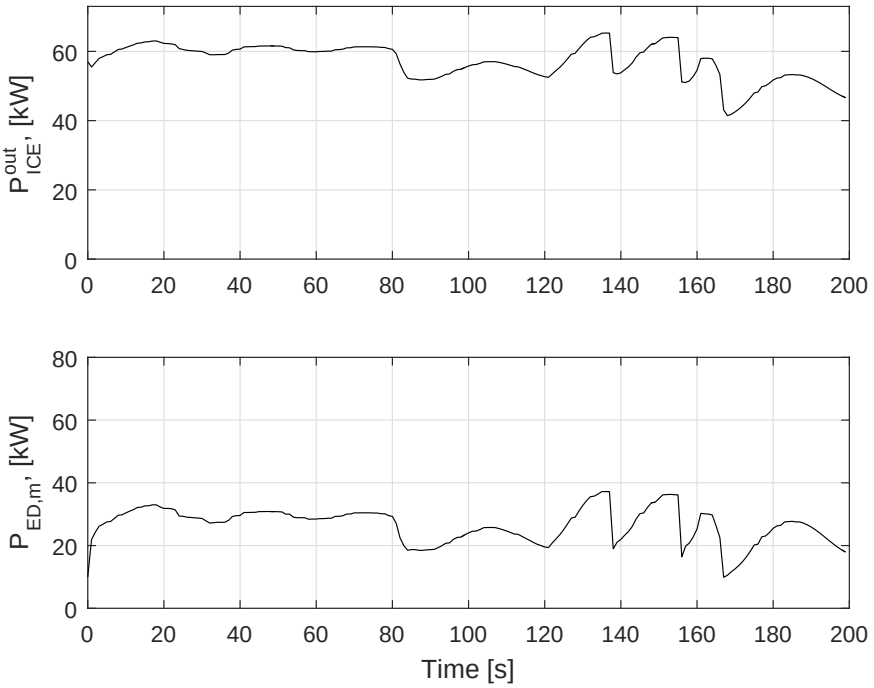

Figure 4.9: ICE and ED mechanical power delivered to the propeller

decrease $\overline{W}_{Bat}$ faster.

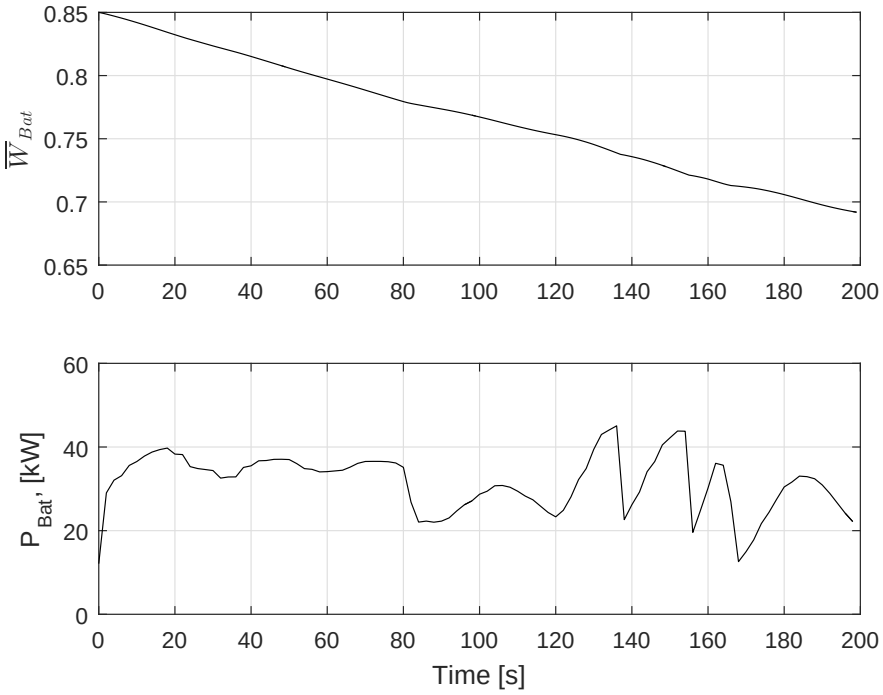

Figure 4.10: Battery state of charge and power draw.

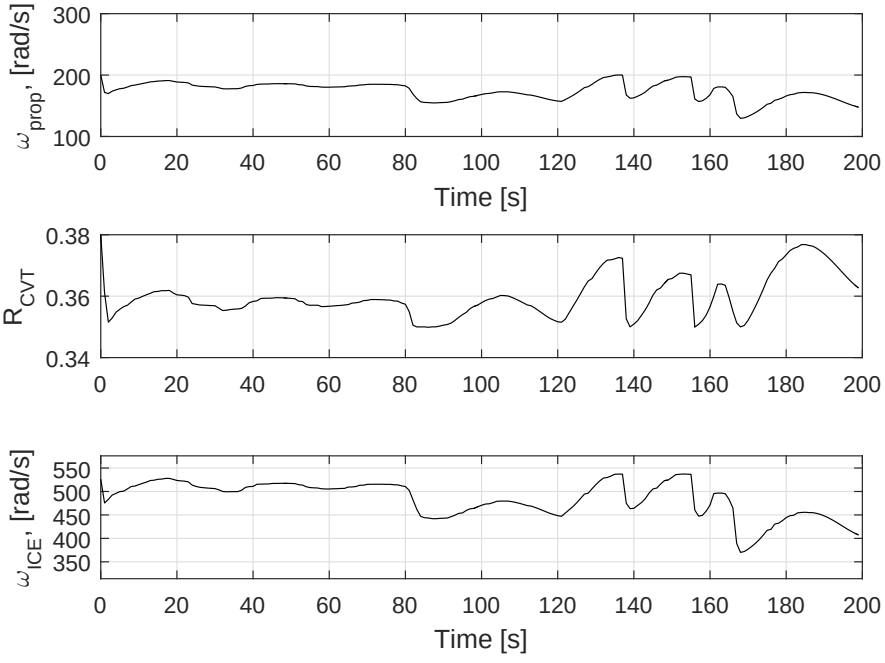

Figure 4.11: Mechanical bus and ICE operation; propeller speed, CVT gear ratio, and ICE speed (top to bottom)

Figure 4.12 demonstrates the λ values as a function of time during the sawtooth profile. Notice that there is no mode switch as the $\overline{W}_{Bat}$ never falls below the desired level of 0.6. Therefore, λ_1 provides the unique system dynamics in order to achieve the desired tracking for the entire flight. Figure 4.12 does provide both the embedded and projected mode values. While there are instances where the embedded system does deviate from $\tilde{\lambda}_1 = 1$ at different times, the projected mode λ remains 1 because the battery penalty never becomes active in the simulation. However, one would expect that as the battery penalty does increase, the embedded system would start to transition to λ_2 once $\overline{W}_{Bat}$ reaches a critical level, this is demonstrated in the next section. An analysis of the effect of adding a fuel penalty is considered in the following section for the sawtooth simulation.

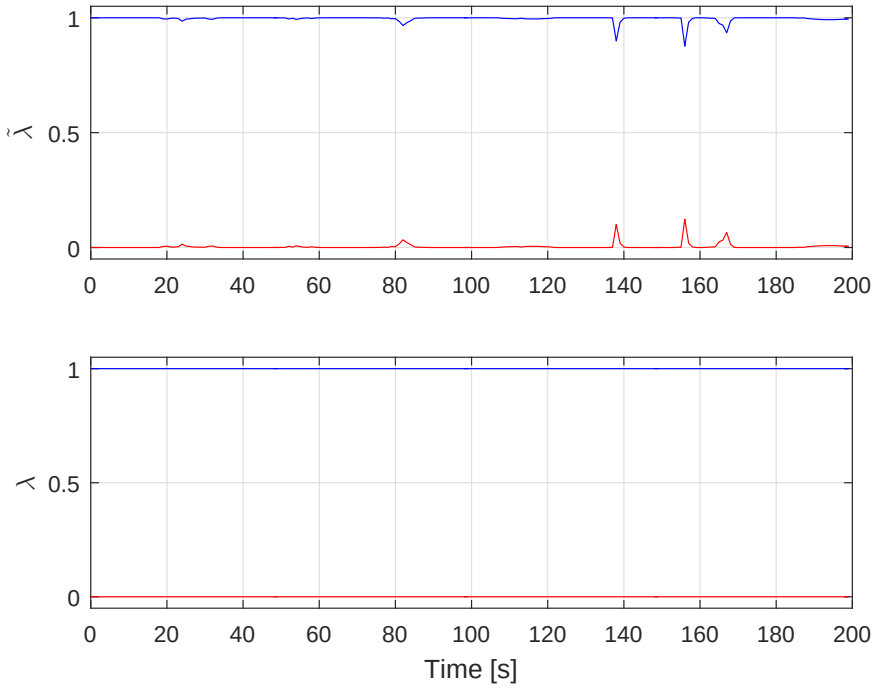

Figure 4.12: Embedded mode values (—) $\tilde{\lambda}_1$ (—) $\tilde{\lambda}_2$, and projected mode values (—) λ_1 (—) λ_2 for the sawtooth simulation

The results of the sawtooth simulation to this point dealt with zero $\mu_{P_{ICE}^{fuel}}$ and, like the Validation profile, a fuel penalty analysis is performed for the sawtooth specific profile. As seen in Figure 4.13, the ICE operating points are plotted on the BSFC map of the ROTAX 912iSc Sport. This is in contrast to Figure 4.14 in which $\mu_{P_{ICE}^{fuel}}$ is increased to 0.001. Again, this magnitude is based on the relative impact of the various μ_i in the PI. Too large of a $\mu_{P_{ICE}^{fuel}}$ will cause the

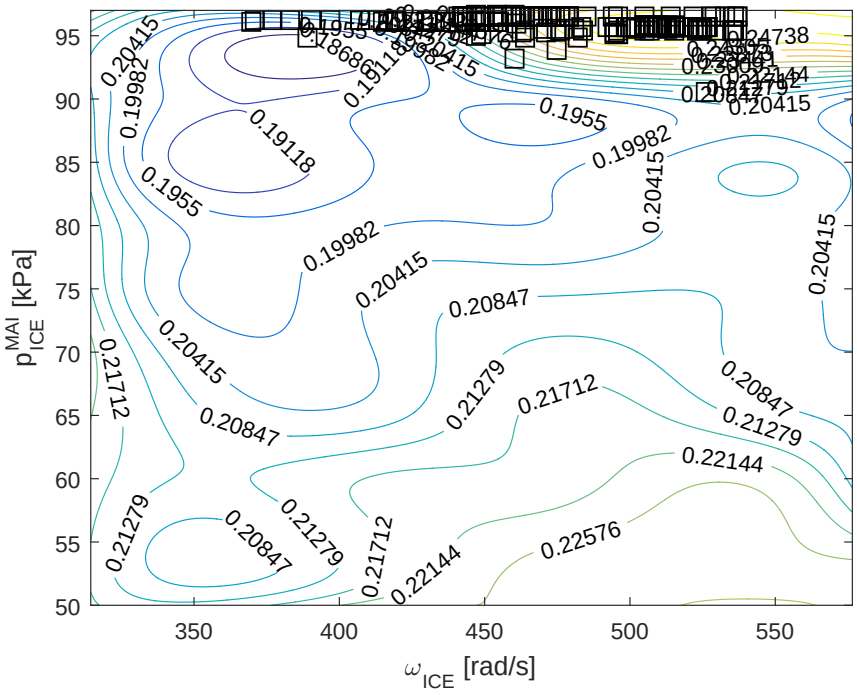

Figure 4.13: ICE operating points over the sawtooth profile with no fuel use penalty

aircraft trajectory to severely diverge from the desired flight profile; the new flight profile is seen in Figure 4.16 which has changed from the trajectory in Figure 4.8 because of the increase in $\mu_{P_{ICE}^{fuel}}$. It is evident in Figure 4.14 that the addition of a fuel penalty has moved the ICE operating points to regions of lower BSFC. Further, as expected, with decreased ICE power in order to operate in more efficient fuel regimes, the ED output mechanical power has increased as seen in Figure 4.15 in order to keep the aircraft on the sawtooth profile. This set of simulation results indicates that the SR-20h can provide increased fuel savings though the MPC strategy developed herein.

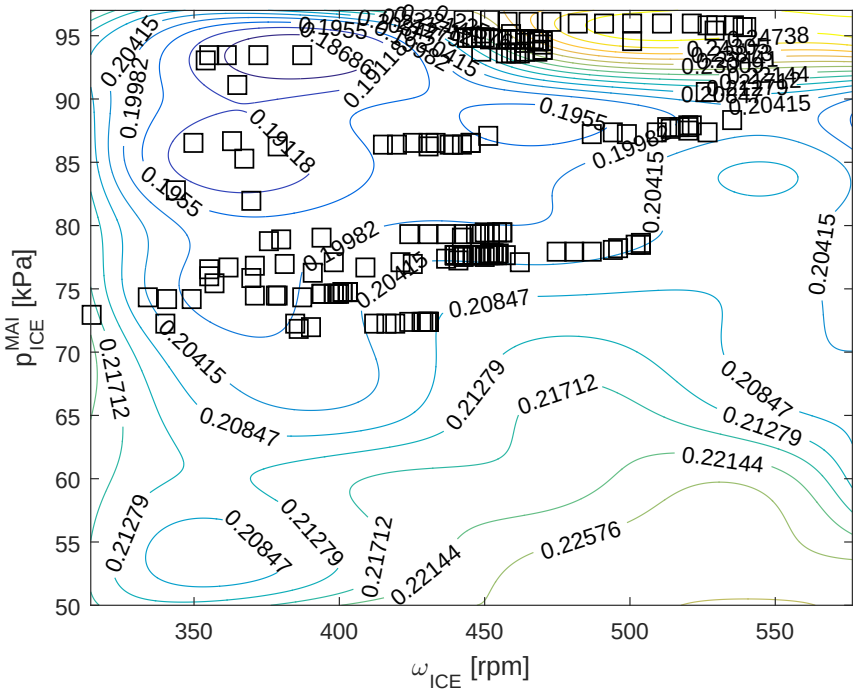

Figure 4.14: ICE operating points over the sawtooth profile which provide high fuel economy

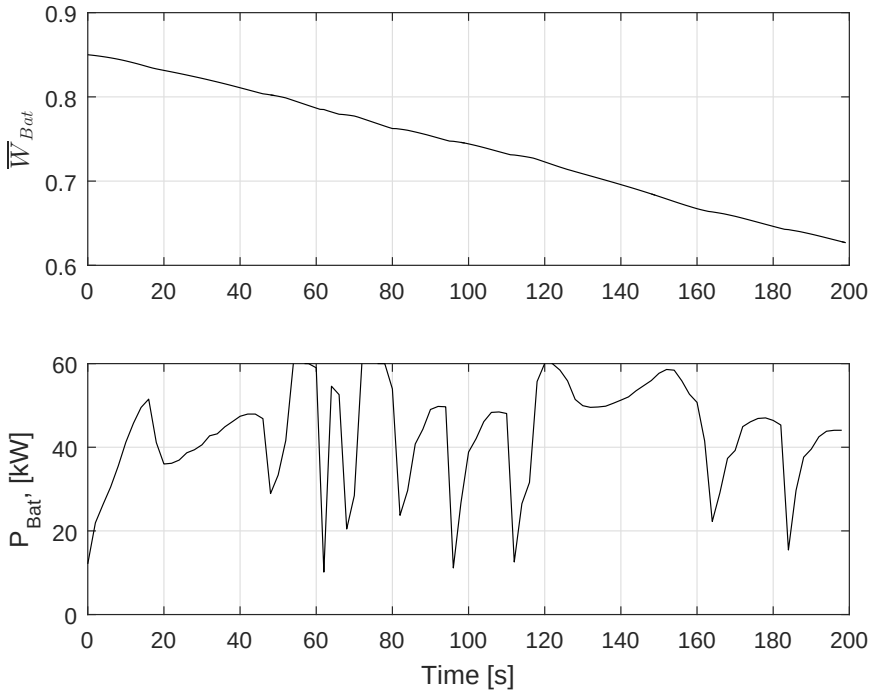

Figure 4.15: Battery use increased as a result of higher fuel economy demand

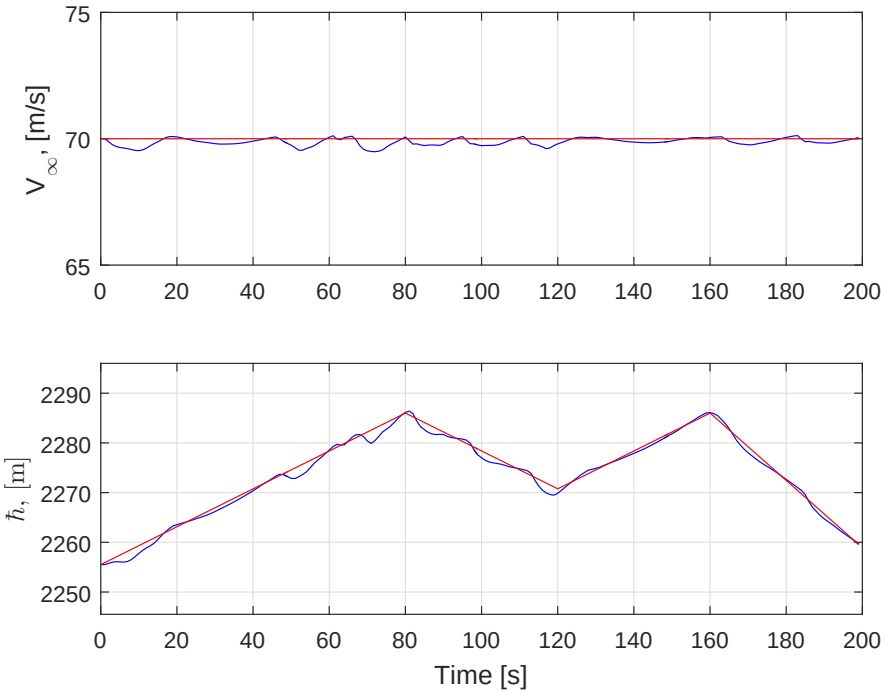

Figure 4.16: Altitude and Velocity tracking with addition of $\mu_{P_{ICE}^{fuel}}$

4.3 Simulation for $\overline{W}_{Bat}$ less than $\overline{W}_{Bat,des}$

The next simulation demonstrates battery charging along with a mode switch. For this simulation, $\mu_{V_\infty} = 600$, $\mu_{\hbar} = 600$, $\mu_{P_{ICE}^{fuel}} = 0$ and μ_{Bat} has the form given in (4.1).

Charging the battery, unique to λ_2, occurs when the battery state of charge deviation cost term in the PI increases to warrant the ICE deviating from a fuel efficient operating point to provide additional power to charge the battery through the ED acting as a generator. Also resulting from the increased μ_{Bat}, velocity and altitude tracking would suffer and the 2-norm error would increase until the battery is at a satisfactory $\overline{W}_{Bat}$ in which the altitude and velocity tracking could resume to minimize the PI.

An example of this situation is observed in Figure 4.17 where the SR-20h is simulated to follow a steady-level flight path. $\overline{W}_{Bat}$ is initially set at 0.5 which is below $\overline{W}_{Bat,des}$ value of 0.6. The aircraft immediately switches to λ_2 and charges the battery as seen in Figure 4.18 until $\mu_{Bat} = 0$. As the difference between the battery state-of-charge and desired state-of-charge decreases, altitude and velocity tracking improve until the steady state flight condition is met.

$\mu_{P_{ICE}^{fuel}}$ is not active in this simulation as the concern in this simulation is to demonstrate that the HEP system is capable of recharging based on the system conditions given. This simulation has a specific relationship for the battery penalty in order to expose the ability of λ_2 by giving large values of μ_{Bat}

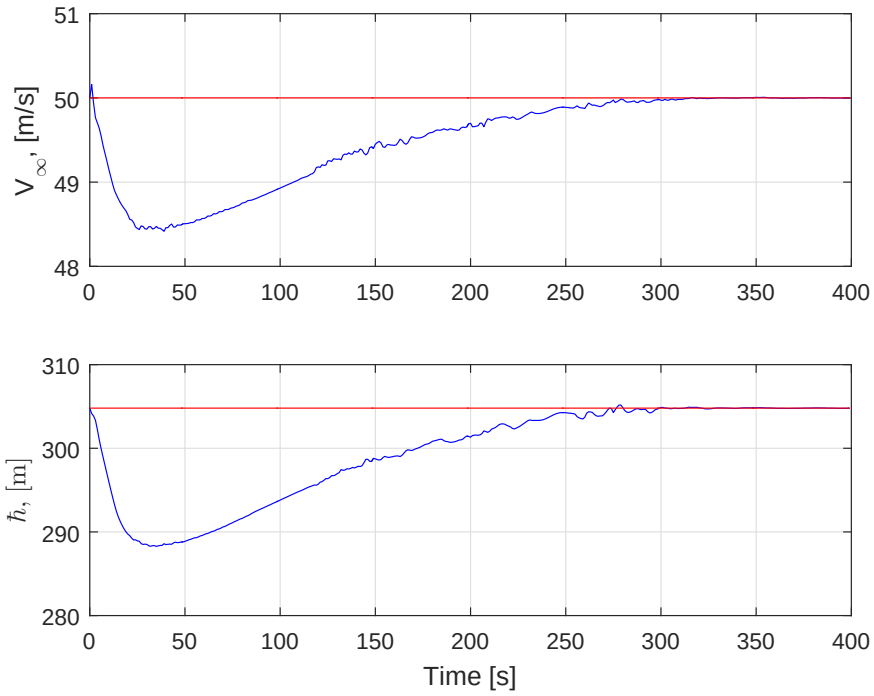

Figure 4.17: Altitude and Velocity as $\overline{W}_{BAT}$ increases for battery charging: (—) simulated trajectory, (—) desired trajectory

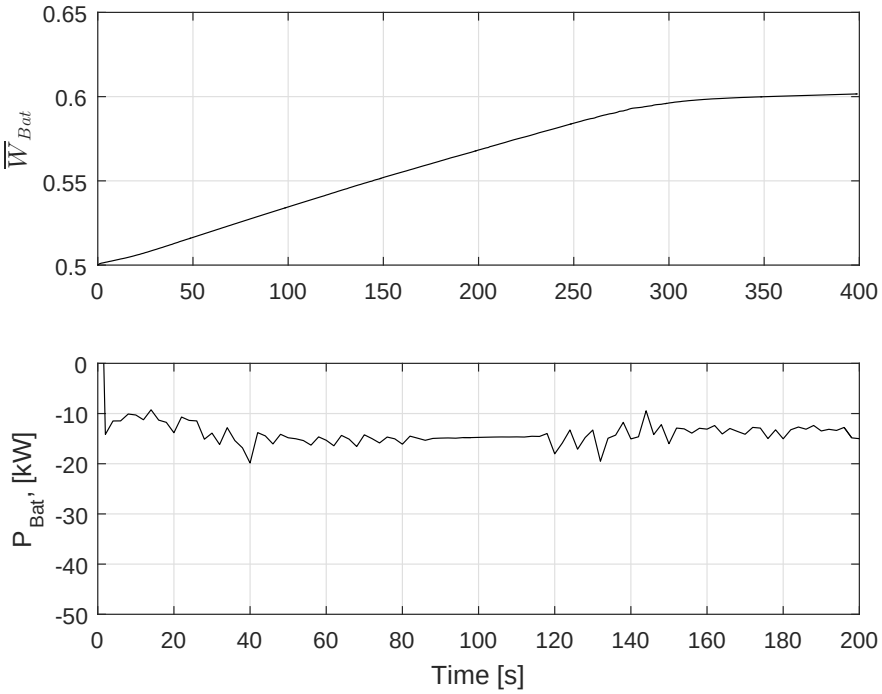

Figure 4.18: $\overline{W}_{BAT}$ charging to desired level; P_{Bat} is negative as defined due to charging model

4.4 Flight Simulation for Obtaining Specific Range

GA aircraft, like the SR-20, often spend the majority of their flight in cruise at a steady-level condition. Further, an optimum speed, $V_{\frac{L}{D}\ max}$ is the speed at which drag is a minimum. There are other associated optimum speeds for maximum endurance and range as well. A steady-level flight scenario is simulated in so that fuel savings can be compared to data available in the SR-20 POH in terms of specific range [kilometers per liter] and also compared to flight test data.

At sea level condition and V_∞ of 68 m/s (127 knots), the specific range from the SR-20 POH is approximately 15.2 nautical miles per gallon; 7.4 km/liter [66]. Other associated speeds and altitudes to achieve the best fuel economy for the SR-20 are given in Figure 4.19. The SR-20h is simulated over a straight-level flight profile at the flight speed given for this metric in the POH, except for $V_\infty = V_{\frac{L}{D}\ max} = 50$ m/s.

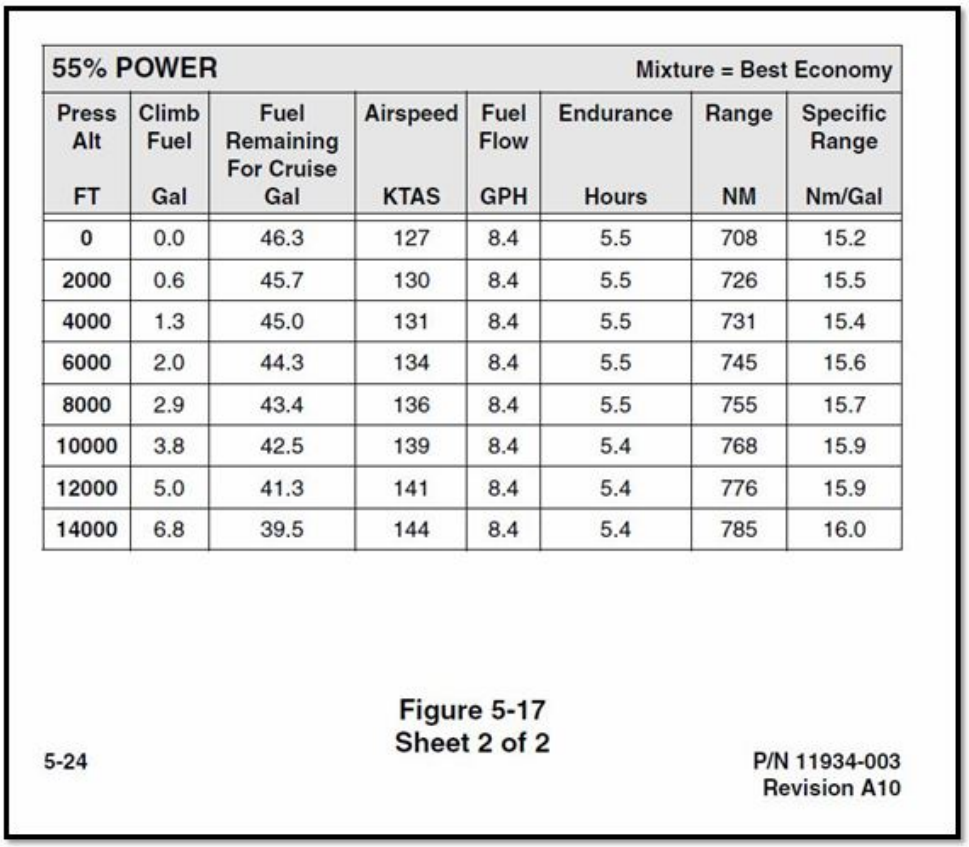

55% POWER — Mixture = Best Economy

Press Alt FT	Climb Fuel Gal	Fuel Remaining For Cruise Gal	Airspeed KTAS	Fuel Flow GPH	Endurance Hours	Range NM	Specific Range Nm/Gal
0	0.0	46.3	127	8.4	5.5	708	15.2
2000	0.6	45.7	130	8.4	5.5	726	15.5
4000	1.3	45.0	131	8.4	5.5	731	15.4
6000	2.0	44.3	134	8.4	5.5	745	15.6
8000	2.9	43.4	136	8.4	5.5	755	15.7
10000	3.8	42.5	139	8.4	5.4	768	15.9
12000	5.0	41.3	141	8.4	5.4	776	15.9
14000	6.8	39.5	144	8.4	5.4	785	16.0

Figure 5-17
Sheet 2 of 2

5-24

P/N 11934-003
Revision A10

Figure 4.19: Fuel economy for the Cirrus SR-20; reproduced from the POH [66]

The simulation time of the level flight is roughly one half hour so that the specific range for the SR-20h is calculated over many kilometers rather than a a few kilometers providing a more accurate comparison.The simulation flight profile trajectory is given in Figure 4.20. Because of the long simulation time, the data displayed in Figure 4.20 is compacted but still results in excellent tracking for which the 2-norm error for velocity and altitude are 0.54% and 0.58%, respectively.

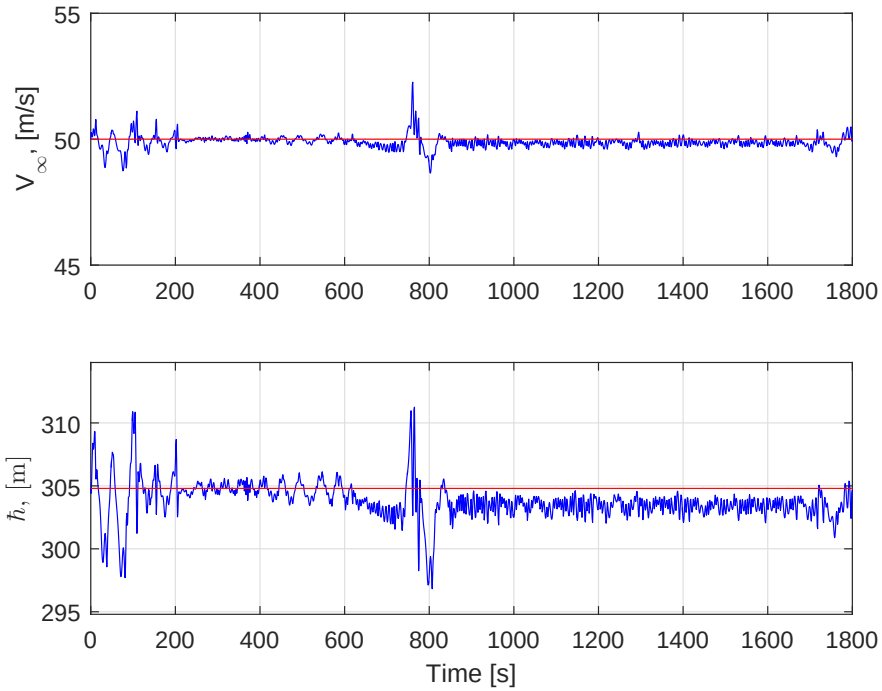

Figure 4.20: Simulated V_∞ and $\hbar$ over the endurance flight profile: (—) simulated trajectory, (—) desired trajectory.

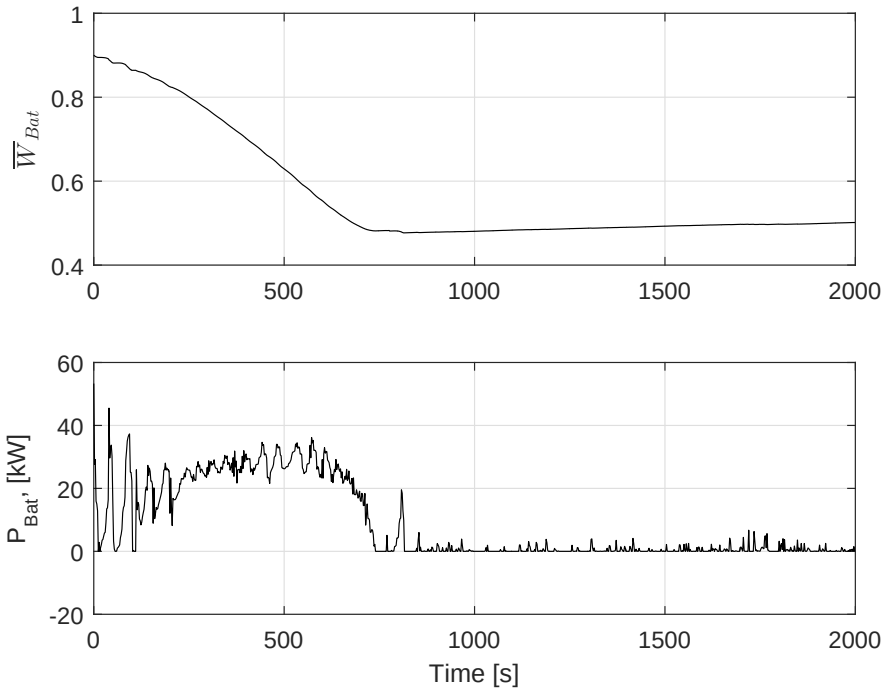

Figure 4.21: $\overline{W}_{Bat}$ and P_{Bat} over the endurance profile; Penalties and component sizing not promoting charging for simulation.

The operation of the ED system is given in Figure 4.21. A stark observation is made in the fact that not only does $\overline{W}_{Bat}$ fall below the desired level, but also the system never promotes battery charging. That is, once $\overline{W}_{Bat}$ reaches a value in the cost function where charging the battery, by extracting power from the ICE, would have a negative impact on altitude and velocity tracking, which would increase the PI value. Further analysis and testing revealed that the cause of the inability to recharge on this simulation is due to not only the relative scale of the μ_i, but also that the ICE is undersized. The ROTAX 912iSc Sport was chosen because it, combined with the ED maximum output powers, replicated the SR-20 Continental ICE output power. Also, the operators manual for the ROTAX 912iSc Sport [55] contained the data necessary to develop a supervisory-level model for use in this work; a variety of ICEs were studied, and the 912iSc Sport was found to have the adequate weight, power, and efficiency model to further develop for this work. This leads to the conclusion that higher powered ICEs are needed beyond a 50% hybridization factor. For example, the turbocharged ROTAX 915iSc Sport, released in Fall 2017, delivers 100 kW vs the 72 in the 912iSc Sport. The 915iSc Sport operators manual was not published at the time of

the selection of component models so the 912iSC Sport was chosen instead as the data and initial study suggested it as a viable ICE for the HEP system herein.

No fair comparison can be made between the SR-20 and SR-20h specific range because battery charging requires power being delivered from the ICE while maintaining flight and therefore increase fuel consumption to a higher value than calculated. Finally, the embedded and projected mode values are given in Figure 4.22. This figure indicates that the embedded system does consider instances where it is less optimal to operate in λ_1, however, the mode projection algorithm in (3.16) results in λ_1 dominating the entire endurance profile. With a larger ICE, like the ROTAX 915iSc Sport, and further tuning of the μ_i in the PI, it is expected that the endurance profile comparisons between the SR-20 and SR-20h could be conducted as well as expansions to simulations of flight test data profiles.

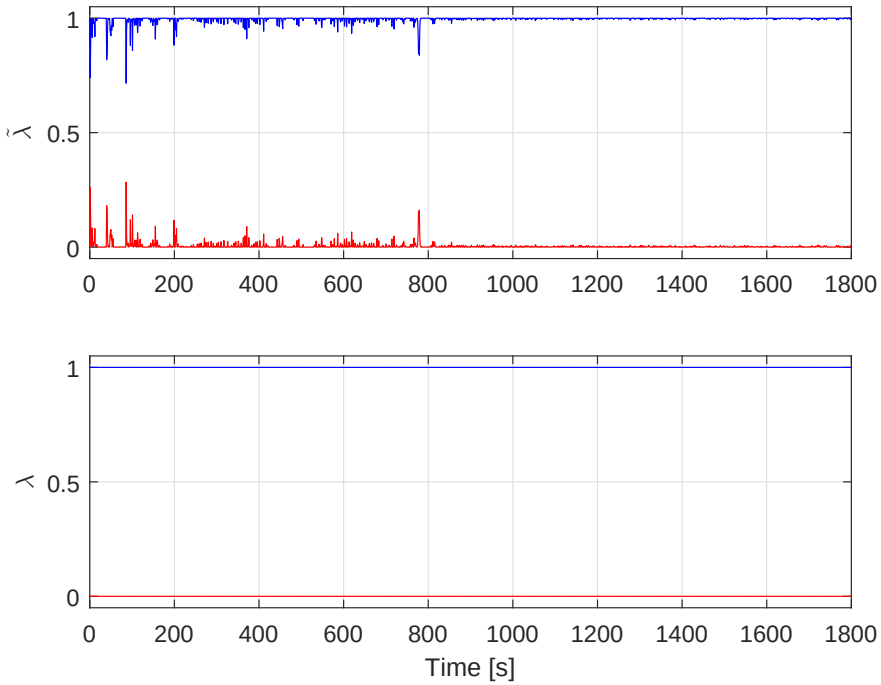

Figure 4.22: Embedded mode values (—) $\tilde{\lambda}_1$ (—) $\tilde{\lambda}_2$, and projected mode values (—) λ_1 (—) λ_2 for the endurance simulation

.

CHAPTER 5

CONCLUSION

This thesis has presented the implementation of a model predictive power management of a hybrid electric propulsion system for aircraft. The model is presented as a supervisory-level model whose dynamics, constraints, and interconnections are discretized for use in an embedding technique to optimally solve the switched system control problem. This unique approach, while studied and documented for automotive applications, has yet to reach maturity in the aeronautical field. This work has provided the basis for several future expansions to occur.

A survey of the literature in this field indicates that HEP technology has gained momentum in recent years as several demonstration aircraft and companies have begun investments into the technology with several under development at the time of writing. There are many similarities that exist between automotive and aircraft hybrid propulsion system such as the architecture in which components such as the ICE, ED, and battery are connected. Modeling of those components can be accomplished in a variety of way but are most often adopted from methods used for terrestrial vehicle hybrid systems or in the form of look-up tables. Rule-Based and Artificial Neural Network system control have shown to offer favorable power management and energy savings within these systems. Traditional methods of formulating aircraft performance and design parameters are affected by HEP and are addressed by transitioning to a power-based design approach. Research and development in the field of HEP for aircraft to-date has provided a strong foundation for future work as further studies and experiments are necessary before widespread hybrid electric aircraft enter the mainstream aviation community.

A HEP system and aircraft model for use in the GA segment is developed. The power system consists of a ROTAX 912iSc Sport engine, a UQM PowerPhase 100 electric motor system, a Lithium-ion battery pack, and a CVT transmission. Each of these components are mathematically modeled as either an algebraic power source/sink or as a dynamic model. Connections between the

components, as well as the equations of motion for an aircraft are given as well. The defined HEP system is paired to an aircraft based on the Cirrus SR-20. Last, the constant speed propeller model, the link between the propulsion system and the aircraft, provides power, velocity, and angular velocity relationships.

Next, a background and methodology of model predictive control for a hybrid system is presented as is tailored for the system model defined in this work. The HEP components and aircraft models form a switched system which operates in one of two modes: (i) battery discharging and ED propelling and (ii) battery charging and ED generating. Mode-specific dynamics, control inputs, and algebraic power variables, along with a unique optimal power performance index is defined. An embedded mode projection algorithm allows the continuous time and nonlinear HEP model to be discretized using collocation. The optimal control solutions are projected to the continuous time system which provide the switched mode optimal hybrid power flow based on system performance objectives and constraints.

Finally, a variety of simulations are performed which prove the feasibility of the control methodology employed in the defined hybrid aircraft model. Climb, descent, and level flight profile simulations showed excellent tracking and appropriate responses by the system components. The effect of increased fuel penalties, i.e. promoting reduced fuel consumption, was demonstrated for the ROTAX 912iSc Sport ICE. Additional simulations were performed which tested the robustness of the HEP system and was found to agree with the logic on how the HEP system operates in this work. Therefore, this work has proven that optimal power flow of a switched HEP system for aircraft does provide fuel savings while achieving the same flight performance as a non-hybrid aircraft.

5.1 Future Work and Outlook

As the first known implementation of this control approach to hybrid propulsion for aircraft, many opportunities exist for improved modeling, flight simulation, and ground testing to not only support these findings, but also advance the technology in industry to a mature level for implementation in aircraft.

Further work is needed in the selection of μ_i in the PI to understand their relative impor-

tance on fuel savings and desired trajectory tracking. Variations in the formulation of the PI may lead to improved system efficiency and operation, such as adding a negative cost term for battery recharging to promote recharging above the desired sate-of-charge when the flight profile allows for it. Also, the ICE, ED, and battery sizing power sizing offers an optimization opportunity to provide insight to the HEP system optimum component weight, power output, and energy storage potential. Based on the results presented, higher powered, or higher energy density components could address the lack of mode switching and power trends of the ICE and ED.

Outside of the ED and battery, improvements of the HEP system component models would provide increased accuracy in simulation results. Further, if available, a full aerodynamic model of an aircraft for use in a six degree of freedom simulator would provide a better representation of the flight loads and demands at the propulsion system. The propeller modeled herein was based on typical performance curves, where aerodynamic modeling or specific propeller manufacturer data would increase the simulation accuracy as the thrust demands at the propeller directly relate to the demands of the HEP system.

One of the initial goals of this thesis was to simulate the SR-20h over physical flight test experiments to provide a comprehensive simulation and initial representation of the effect between non-hybrid and hybrid aircraft propulsion systems. With the discovery of the ICE performance not sufficient to charge the battery over long endurance and flight test experiments, further studies into larger ICE modeling and simulations using the developed flight test data established early in this work schedule are needed.

This work offers insight into a new method of system control which has seen widespread adoption in the automotive world and can be argued to have as similar, if not larger, impact on the aerospace community. To address the stringent performance goals for current and future aircraft, HEP aircraft offer to be the stepping stone full electrified flight. This research has demonstrated that this technology has strong interest in the aviation community and that further expansions of model predictive control of switched hybrid aircraft propulsion systems should be pursued.

REFERENCES

[1] Lu, C. and Morrell, P., "Determination and applications of environmental costs at different sized airports–aircraft noise and engine emissions," *Transportation*, Vol. 33, No. 1, 2006, pp. 45–61.

[2] Holtberg, P., "Annual Energy Outlook 2012 with Projections to 2035," Tech. rep., United States Energy Information Administration, Washington, DC, 2012.

[3] Luongo, C. A., Masson, P. J., Nam, T., Mavris, D., Kim, H. D., Brown, G. V., Waters, M., and Hall, D., "Next generation more-electric aircraft: a potential application for HTS superconductors," *Applied Superconductivity, IEEE Transactions on*, Vol. 19, No. 3, 2009, pp. 1055–1068.

[4] Jagannath, R., Bane, S., Nalim, M. R., and Khan, J., "A Simplified Method To Calculate The Fuel Burn Of A Hybrid-Electric Airplane," *50th AIAA/ASME/SAE/ASEE Joint Propulsion Conference*, 2014, p. 3490.

[5] Peters, D. A. and McKay, D. R., "The current decline in oil: Investment and macroeconomic considerations," *Plastic surgery*, Vol. 23, No. 1, 2014, pp. 55–56.

[6] Pornet, C. and Isikveren, A., "Conceptual design of hybrid-electric transport aircraft," *Progress in Aerospace Sciences*, Vol. 79, 2015, pp. 114–135.

[7] Caldecott, S., "General Aviation Statistical Databook and 2017 Industry Outlook," Tech. rep., General Aviation Manufacturers' Association, Washington, DC, 2016.

[8] Friedrich, C. and Robertson, P. A., "Design of a Hybrid-Electric Propulsion System for Light Aircraft," *AIAA AVIATION 2014-14th AIAA Aviation Technology, Integration, and Operations Conference*, AIAA, 2014.

[9] Mi, C., Masrur, M. A., and Gao, D. W., *Hybrid electric vehicles: principles and applications with practical perspectives*, John Wiley & Sons, 2011.

[10] Friedrich, C. and Robertson, P. A., "Hybrid-electric propulsion for aircraft," *Journal of Aircraft*, Vol. 52, No. 1, 2014, pp. 176–189.

[11] Moore, M. D. and Fredericks, B., "Misconceptions of electric propulsion aircraft and their emergent aviation markets," *52nd Aerospace Sciences Meeting AIAA SciTech*, Vol. 17, 2014.

[12] Blee, S., "Aviation Photo 2473443 Diamond DA-36 E-Star - Diamond Aircraft Industries," Airliners.net, December 2014.

[13] Harmats, M. and Weihs, D., "Hybrid-propulsion high-altitude long-endurance remotely piloted vehicle," *Journal of Aircraft*, Vol. 36, No. 2, 1999, pp. 321–331.

[14] Harmon, F. G., Frank, A. A., and Joshi, S. S., "Application of a CMAC neural network to the control of a parallel hybrid-electric propulsion system for a small unmanned aerial vehicle," *Neural Networks, 2005. IJCNN'05. Proceedings. 2005 IEEE International Joint Conference on Neural Networks*, Vol. 1, IEEE, 2005, pp. 355–360.

[15] Harmon, F. G., Frank, A. A., and Joshi, S. S., "The control of a parallel hybrid-electric propulsion system for a small unmanned aerial vehicle using a CMAC neural network," *Neural Networks*, Vol. 18, No. 5, 2005, pp. 772–780.

[16] Harmon, F. G., *Neural network control of a parallel hybrid-electric propulsion system for a small unmanned aerial vehicle*, Ph.D. thesis, University of California Davis, 2005.

[17] Harmon, F. G., Frank, A. A., and Chattot, J.-J., "Conceptual design and simulation of a small hybrid-electric unmanned aerial vehicle," *Journal of aircraft*, Vol. 43, No. 5, 2006, pp. 1490–1498.

[18] Hiserote, R. and Harmon, F., "Analysis of hybrid-electric propulsion system designs for small unmanned aircraft systems," *8th Annual International Energy Conversion Engineering Conference*, 2010, p. 6687.

[19] Hung, J. and Gonzalez, L. F., "On parallel hybrid-electric propulsion system for unmanned aerial vehicles," *Progress in Aerospace Sciences*, Vol. 51, 2012, pp. 1–17.

[20] Righi, H., *Hybrid electric aircraft*, Master's thesis, Mississippi State University, 2016.

[21] Cipolla, V. and Oliviero, F., "HyPSim: A Simulation Tool for Hybrid Aircraft Performance Analysis," *Variational Analysis and Aerospace Engineering*, Springer, 2016, pp. 95–116.

[22] Fletcher, S., Flynn, M.-C., Jones, C. E., and Norman, P. J., "Hybrid Electric Aircraft: State of the Art and Key Electrical System Challenges," *Newsletter*, 2016.

[23] Bradley, M. K. and Droney, C. K., "Subsonic Ultra Green Aircraft Research," Tech. rep., NASA, May 2012.

[24] Pornet, C., Gologan, C., Vratny, P. C., Seitz, A., Schmitz, O., Isikveren, A. T., and Hornung, M., "Methodology for sizing and performance assessment of hybrid energy aircraft," *Journal of Aircraft*, Vol. 52, No. 1, 2014, pp. 341–352.

[25] Adams, E., "Zunums Hybrid Jet Could Finally Make Electric Flight a Reality," *WIRED Transportation*, 2017.

[26] Lents, C. E., Hardin, L. W., Rheaume, J., and Kohlman, L., "Parallel Hybrid Gas-Electric Geared Turbofan Engine Conceptual Design and Benefits Analysis," *52nd AIAA/SAE/ASEE Joint Propulsion Conference*, 2016, p. 4610.

[27] Greiser, C. M., Mengistu, I. H., Rotramel, T. A., and Harmon, F. G., "Testing of a Parallel Hybrid-Electric Propulsion System for use in a Small Remotely-Piloted Aircraft," *9th AIAA Annual International Energy Conversion Engineering Conference*, 2011.

[28] Olsen, J., Page, J., and Ahmed, N.-E., "A hybrid propulsion system for a light trainer aircraft," *AIAC15: 15th Australian International Aerospace Congress*, Australian International Aerospace Congress, 2013, p. 637.

[29] Lukic, S. M. and Emadi, A., "Effects of drivetrain hybridization on fuel economy and dynamic performance of parallel hybrid electric vehicles," *IEEE transactions on vehicular technology*, Vol. 53, No. 2, 2004, pp. 385–389.

[30] Schoemann, J. and Hornung, M., "Modeling of Hybrid-Electric Propulsion Systems for Small Unmanned Aerial Vehicle," *Proceedings of 12th AIAA Aviation Technology, Integration, and Operations (ATIO) Conference and 14th AIAA/ISSM*, 2012, pp. 17–19.

[31] Schömann, J., *Hybrid-electric propulsion systems for small unmanned aircraft*, Master's thesis, Technische Universität München, 2014.

[32] Hung, J. Y. and Gonzalez, L. F., "Design, simulation and analysis of a parallel hybrid electric propulsion system for unmanned aerial vehicles," *Proceedings of the 28th International Congress of the Aeronautical Sciences, Optimage Ltd., Brisbane Convention & Exhibition Centre, Brisbane, QLD, pp. 1-13*, 2012.

[33] Hung, J. Y.-C., *Investigation of methods for increasing the energy efficiency on unmanned aerial vehicles (UAVS)*, Master's thesis, Queensland University of Technology, 2011.

[34] Meyer, R. T., DeCarlo, R. A., Meckl, P. H., Doktorcik, C., and Pekarek, S., "Hybrid Model Predictive Power Management of A Fuel Cell-Battery Vehicle," *Asian Journal of Control*, Vol. 15, No. 2, 2013, pp. 363–379.

[35] Meyer, R. T., DeCarlo, R. A., and Pekarek, S., "Hybrid Model Predictive Power Management of a Battery-Supercapacitor Electric Vehicle," *Asian Journal of Control*, Vol. 18, No. 1, 2016, pp. 150–165.

[36] McDonald, R. A., "Electric Propulsion Modeling for Conceptual Aircraft Design," *52nd Aerospace Sciences Meeting*, 2014, p. 0536.

[37] Rößler, C. O., *Conceptual design of unmanned aircraft with fuel cell propulsion system*, Verlag Dr. Hut, 2012.

[38] Aktas, D., "General Aviation Electric-Powered Aircraft Feasibility," *50th AIAA Aerospace Sciences Meeting including the New Horizons Forum and Aerospace Exposition*, 2012, p. 1040.

[39] Agarwal, V., Uthaichana, K., DeCarlo, R. A., and Tsoukalas, L. H., "Development and validation of a battery model useful for discharging and charging power control and lifetime estimation," *IEEE Transactions on Energy Conversion*, Vol. 25, No. 3, 2010, pp. 821–835.

[40] Thauvin, J., Barraud, G., Budinger, M., Roboam, X., Leray, D., and Sareni, B., "Hybrid regional aircraft: a comparative review of new potentials enabled by electric power," *52nd AIAA/SAE/ASEE Joint Propulsion Conference*, 2016, p. 4612.

[41] Lieh, J., Spahr, E., Behbahani, A., and Hoying, J., "Design of hybrid propulsion systems for unmanned aerial vehicles," *17th AIAA International Space Planes and Hypersonic Systems and Technologies Conference*, 2011.

[42] Stevens, B. L., Lewis, F. L., and Johnson, E. N., *Aircraft control and simulation: dynamics, controls design, and autonomous systems*, John Wiley & Sons, 2015.

[43] Schmidt, L. V., *Introduction to aircraft flight dynamics*, AIAA, 1998.

[44] Etkin, B. and Reid, L. D., *Dynamics of flight: stability and control*, Vol. 3, Wiley, New York, 1996.

[45] Thong, C. W., "Modeling Aircraft Performance and Stability on X-Plane," *Australian Defence Force Academy, Univ. of New South Wales, Canberra, Australia*, 2010.

[46] Anderson, J. D., *Aircraft performance and design*, Vol. 1, WCB/McGraw-Hill Boston, 1999.

[47] Raymer, D. P., *Aircraft Design: A Conceptual Approach*, AIAA, 2012.

[48] Hepperle, M., "JAVAPROP-USERS GUIDE," 2010, Software Package, Braunschweig, Germany: available online at http://www.mh-aerotools.de/airfoils/index .htm.

[49] Karunarathne, L., Economou, J. T., and Knowles, K., "Fuzzy logic control strategy for fuel cell/battery aerospace propulsion system," *2008 IEEE Vehicle Power and Propulsion Conference*, IEEE, 2008, pp. 1–5.

[50] Meyer, R. T. and Revankar, S., "A survey of PEM fuel cell system control models and control developments," *ASME 2006 4th International Conference on Fuel Cell Science, Engineering and Technology*, American Society of Mechanical Engineers, 2006, pp. 63–79.

[51] Nam, T., Soban, D. S., and Mavris, D. N., "Power based sizing method for aircraft consuming unconventional energy," *43rd AIAA Aerospace Sciences Meeting and Exhibit*, 2005, pp. 2005–0818.

[52] Hepperle, M., "Electric Flight-Potential and Limitations," *AVT-209 Workshop on energy efficicent technologies and concepts operation*, 2012.

[53] Bagassi, S., Bertini, G., Francia, D., and Persiani, F., "Design Analysis for Hybrid Propulsion," *Proceedings of the 28th International Congress of the Aeronautical Sciences (ICAS 2012)*, Vol. 873, 2015.

[54] Traub, L. W., "Range and endurance estimates for battery-powered aircraft," *Journal of Aircraft*, Vol. 48, No. 2, 2011, pp. 703–707.

[55] Bombardier Recreational Products (BRP), Gunskirchen, Austria, *Operators Manual ROTAX 912 i Series*, 2nd ed., 2015.

[56] Lang, C., "Power output of a Rotax 914 with c/s prop," Rotary Wing Forum.

[57] Grzegożek, W. and Szczepka, M., "Analysis of an employment of a gear ratio rate in CVT control system," *IOP Conference Series: Materials Science and Engineering*, Vol. 148, IOP Publishing, 2016, p. 012007.

[58] Shabrov, N., Ispolov, Y., and Orlov, S., "Simulations of continuously variable transmission dynamics," *ZAMM-Journal of Applied Mathematics and Mechanics/Zeitschrift für Angewandte Mathematik und Mechanik*, Vol. 94, No. 11, 2014, pp. 917–922.

[59] Meyer, R. T., DeCarlo, R. A., Jali, N. M., and Ariyur, K. B., "Behavioral modeling and optimal control of a vehicle mechanical drive system," *American Control Conference (ACC), 2015*, IEEE, 2015, pp. 2266–2271.

[60] Nelson, R. C., *Flight stability and automatic control*, Vol. 2, WCB/McGraw Hill New York, 1998.

[61] Roskam, J., *Airplane design*, DARcorporation, 1985.

[62] Kapseong, R., "AE 3800 - Flight Vehicle Performance," 2014.

[63] Kapseong, R., "AE 6400 - Aircraft Stability and Control," 2014.

[64] "Type Certificate Data Sheet NO. A00009CH," Tech. rep., Federal Aviation Administration, 2017.

[65] "Type Certificate Data Sheet NO. E1CE," Tech. rep., Federal Aviation Administration, 2017.

[66] "Pilots Operating Handbook and FAA Approved Airplane Flight Manual for the Cirrus Design SR20," Manual, Cirrus Design Corp., Duluth, MN, October 2003.

[67] "Type Certificate Data Sheet NO. P36EA," Tech. rep., Federal Aviation Administration, 2017.

[68] Hamilton-Strundstad, "Generalized Method of Propeller Performance Estimation," Tech. rep., Boston University, Windsor Locks, CT, 1963.

[69] Rossiter, J. A., *Model-based predictive control: a practical approach*, CRC press, 2003.

[70] Camacho, E. F. and Bordons, C., *Model predictive control in the process industry*, Springer Science & Business Media, 2012.

[71] Bao-Cang, D., *Modern predictive control*, CRC press Boca Raton, USA, 2010.

[72] Meyer, R., "ME 5620 - Application of Numerical Methods in Engineering," 2015.

[73] Meyer, R. T., Zefran, M., and DeCarlo, R. A., "A comparison of the embedding method with multiparametric programming, mixed-integer programming, gradient-descent, and hybrid minimum principle-based methods," *IEEE Transactions on Control Systems Technology*, Vol. 22, No. 5, 2014, pp. 1784–1800.

[74] Bengea, S. C. and DeCarlo, R. A., "Optimal control of switching systems," *Automatica*, Vol. 41, No. 1, 2005, pp. 11–27.

[75] Uthaichana, K., DeCarlo, R. A., Bengea, S. C., Pekarek, S., and Zefran, M., "Hybrid optimal theory and predicitive control for power management in hybrid electric vehicle," *Journal of Nonlinear Systems and Applications*, Vol. 2, No. 1-2, 2011, pp. 96–110.

[76] Von Stryk, D. M. O., "Numerical solution of optimal control problems by direct collocation," *Optimal Control*, Springer, 1993, pp. 129–143.